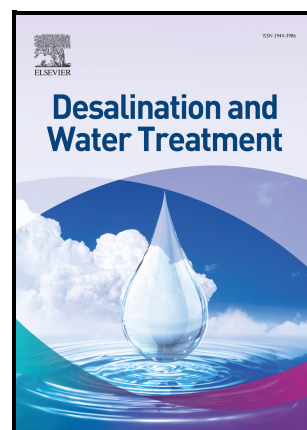# Journal Pre-proof

Cathodic shift in flatband potential of hematite based photoelectrodes: Evaluating and correlating the redshift to solar driven photocatalysis

Atif Zeb, Muhammad Saliman, Abdul Wajid, Hameed Ullah, Tanveer ul Haq Zia

Please cite this article as: Atif Zeb, Muhammad Saliman, Abdul Wajid, Hameed Ullah and Tanveer ul Haq Zia, Cathodic shift in flatband potential of hematite based photoelectrodes: Evaluating and correlating the redshift to solar driven photocatalysis, *Desalination and Water Treatment*, (2024) doi:https://doi.org/10.1016/j.dwt.2024.100792

This is a PDF file of an article that has undergone enhancements after acceptance, such as the addition of a cover page and metadata, and formatting for readability, but it is not yet the definitive version of record. This version will undergo additional copyediting, typesetting and review before it is published in its final form, but we are providing this version to give early visibility of the article. Please note that, during the production process, errors may be discovered which could affect the content, and all legal disclaimers that apply to the journal pertain.

Cathodic shift in flatband potential of hematite based photoelectrodes: Evaluating and correlating the redshift to solar driven photocatalysis

Atif Zeb[1], Muhammad Saliman[1], Abdul Wajid[1], Hameed Ullah**[1], Tanveer ul Haq Zia*[2, 3]

[1]Department of Chemistry, Islamia College Peshawar, 25120 Peshawar, Pakistan

[2] Institute of Chemical Sciences, University of Peshawar, 25120 Peshawar, Pakistan

[3]Government Degree College (Pabbi), Higher Education, Archives and Library Department, KPK, 25120 Peshawar, Pakistan

*Corresponding author: Tanveer ul Haq Zia

E-mail: tanveer.chemistry@suit.edu.pk
Phone/Fax: +92-344-9011757

**Corresponding author: Hameed Ullah

E-mail: hameedullah.wazir@gmail.com

Atif Zeb
atifzeb2017@gmail.com

Muhammad Saliman
Salimank908@gmail.com

Abdul Wajid
wajidchemist943@gmail.com

Abstract

As a promising metal oxide semi-conductor, hematite (α-Fe$_2$O$_3$) has interesting optical properties to be regarded as photoactive material. In this study, we evaluated the cathodic shift in onset potential (E_{onset}) and the negative shift in flat band potential (E_{fb}). It was observed that the E_{onset} value of -0.457 V for α-Fe$_2$O$_3$ based electrode shifted to -0.638 V for the ternary nanocomposite (PNFC) [Pani/Ni-α-Fe$_2$O$_3$/CNT] based electrode. The flat band potential for α-Fe$_2$O$_3$ in 1M NaOH is at -0.49 V which shifts to -0.68 V for the ternary nanocomposite (PNFC). This photoelectrochemical enhancement appears due to electron-hole pair separation. Therefore, it apparently increases the photocurrent trace for PNFC at -0.60 V to 7.04 mA cm^{-2}, compared to the photocurrent of 4.52 mA cm^{-2} observed for pristine α-Fe$_2$O$_3$. According to the Mott-Schottky plot, the donor concentration (N_d) for the α-Fe$_2$O$_3$ is 4.83 x 10^9 cm^{-3}, whereas for the ternary nanocomposite (PNFC) is 7.68 x 10^9 cm^{-3}, respectively. As evident, the N_d value increase for the ternary nanocomposite PNFC points to the proximity of the Fermi (E_f) level below the CB edge when Ni doped α-Fe$_2$O$_3$ comes in contact with polyaniline (Pani). Indeed, the ternary nanocomposite PNFC with lower E_g value (1.32 eV) and higher photocurrent (7.04 mA cm^{-2}) show higher photo-activity with percent degradation of 98.42% for photocatalytic degradation of Sunset Yellow under visible light irradiation. The aforementioned correlations of the energetic levels of band edges with the shifting of E_{fb} to more negative potentials provide insight into the high photo-activity observed.

Keywords

Flatband potential; Photoactive; Ni doping; Mott-Schottky plot; Fermi level; Langmuir-

Hinshelwood model

Introduction

As a sustainable source of energy, the harnessing of solar irradiation has potential that will greatly suffice the ongoing energy demand globally. However, the crucial task here is the development of such semi-conducting materials which are not only efficient but also economically viable for harvesting the radiation energy. Among the attractive possibilities to harness solar energy, photoelectrochemical (PEC) processes are of prime importance. But the key factor for a successful commercial application of PEC based material is the development of photo-active material that fulfil the stern requirements of efficiency and durability [1]. Recently it has been observed that the semiconductor based nanocomposites depict cathodic shift in Fermi levels when subjected to metal ion doping [2, 3]. The enhancement in the composite system energetics then occurs due to the Fermi level shifting towards the more negative potential which also facilitates the interfacial charge-transfer processes. Among the semi-conducting material employed as photo-active material, the electron-hole pair recombination limits their photo activity hence decreasing their efficiency [4]. A subtle approach to address this matter is to couple two different semi-conducting substances which will decrease the recombination rate, hence increasing the efficiency. Benamira et. al developed such an interesting photocatalyst based on a Cu_2O/TiO_2 heterojunction for the photocatalytic degradation of the cationic dye Rhodamine B [5]. According to the Mott-Schottky plots, the flat band potentials were found to be 0.3 and -0.32 V vs SCE for TiO_2 and Cu_2O, respectively, which depicted an enhancement in the photo-electrochemical properties of the as prepared catalyst. Such improvement occurs when two semi-conducting material with the position of the conduction bands (CB) and the valence bands (VB) edges at appropriate levels, can lead to transport of photo-generated charge carriers across the interface which hinders electron-hole pair recombination improving the photo activity which will result in outperforming the activity of each individual semiconductor [6, 7].

The magnetic iron oxide (hematite) (α-Fe$_2$O$_3$) nanoparticles have edge over other semi-conductors of being magnetic in nature rendering it clearly divisible and chemical stability at any range of pH [8]. They are thought to be such materials that carry significant properties such as catalytic behavior, biocompatible nature, low-cost, non toxicity and environmentally benign nature [9]. Hematite (α-Fe$_2$O$_3$) is an n-type semiconductor having an optical band gap of 2.1 eV, respectively [10]. It can utilize visible light energy with wavelengths in visible region upto 600 nm, thus using ~45% of the solar energy radiations. The significant electron–electron interaction is evident in the hematite (α-Fe$_2$O$_3$) in addition to the coupling of the electron–phonon which depicts the complexity of the electronic structures as well as enhanced optical properties. Since, the hematite is environmentally benign whereas is also stable thermodynamically of all the oxides of iron under different pH and ambient environment. Hematite (α-Fe$_2$O$_3$) based nanoparticles have found significant uses solar based catalysts pertaining to the narrow optical band gap [11]. Despite this, the efficiency of semiconductor photocatalysts is limited by photoexcited charge carrier recombination and a confined light absorption zone. Although such photoactive material has been developed in which the charge separation of photogenerated electron-hole (e-/h+) pairs by solar excitation within a depletion width, extended up 15 nm [12]. Therefore, the photogenerated e$^-$ can be transmitted to electrically conducting materials that operate as e$^-$ acceptors, can successfully prevent the photogenerated electron hole pair from recombination. The doping of the conducting polymers such as polypyrrole, polythiophene and polyaniline with suitable dopant such as protonic acid improves its conductivity [13].

Presently, a great curiosity has been revealed by the research community toward electrically conductive polymers, particularly polyaniline (PANI), for their physical and chemical applications. Polyaniline can be constructed as powders, aqueous suspensions and as the polymer matrix for the embedment of the NPs, and it can be involved in different co-

5

polymerization synthesis techniques for enhancing the conductivity of final compounds, such as, by doping polyaniline (PANI) with protonic acid or graphene and carbon nano walls [14]. Moreover, PANI efficiently removes microbes and colorants from waste waters, so, it possesses antibacterial and photocatalytic activity. The advantage of conductive polymers over the conductive materials listed above is their processability, particularly through the solution process. Solar cells, transistors, thermo-electric power sector, microwave absorptive material, and LEDs are just a few of the applications where conductive polymers have been studied extensively [15]. Intrinsically conducting polymers can be combined with semi-conductor nano-assemblies to create composite photocatalysts. Because conducting polymers can match electron energy level geometries with other semiconductor materials, they can minimize photogenerated electron-hole pair interaction in composite photocatalysts. The act of starting a reaction by absorbing light and transferring it to the necessary reactants is the basic step in the process of sensitization. By contributing an electron to the substrate or abstracting hydrogen atom from the substrate, photosensitizes cause a physicochemical change in an adjacent molecule. Various techniques have been used to increase the photocatalytic and photoelectrochemical activities of metal oxide nanostructures, including coupling of graphene derivatives [16], carbon nanotubes [17], and fullerene [18].

Under this study, we performed a systematic investigation for understanding the correlation between the modification of the α-Fe$_2$O$_3$ and that of the photo-optical performance of the ternary nanocomposite PNFC based photoanodes. Of the modification routes at hand, we employed α-Fe$_2$O$_3$ doping with Ni and then performing surface modification with Pani as well as MWCNTs as zero band gap material. Therefore, we also addressed the cathodic shift in E_{onset} and shifting of the E_{fb} in relation to redshift in the optical band gap with post doping modification which effectively improved the photo-optical properties of the ternary nanocomposite PNFC.

Experimental

Materials

Anhydrous salts of iron (II) chloride, iron (III) chloride and nickel (II) nitrate having purity of 99.99% were acquired from Merck. For pH 7, 0.25 M aqueous acetate buffer solution was prepared by mixing with acetic acid or NaOH for pH adjustment with sodium acetate stock standard solution and further diluted with deionized water to attain the required volume. Multi-walled carbon nanotubes (O.D. $\times$ L 6-13 nm $\times$ 2.5-20 μm, >98% (carbon)) were purchased from Sigma Aldrich and were used as it is. The aniline monomer was acquired from the UNI CHEM which was subjected to vacuum distillation prior to use. Ammonium peroxydisulfate (APS) (purity ~98%), was procured from Duksan Pure-Chemicals, South Korea, and was used as it is. Commercial grade methanol and acetone were attained and were purified through distillation under vacuum prior to use.

Synthesis of Doped [Ni-α-Fe$_2$O$_3$] and Undoped Hematite [α-Fe$_2$O$_3$] nanoparticles

Hematite α-Fe$_2$O$_3$ nanoparticles was prepared by employing co-precipitation technique [19]. Initially, the Fe^{3+}/Fe^{2+} mixture in 2:1 was prepared in distilled water while stirring it vigorously for 1 h at 80 °C. Afterwards, the above prepared mixture was basified with dropwise addition of 1M NaOH aqueous solution while stirring for 2 h vigorously. The reactions proceedings were observed with formation dark black brown colored precipitates. Finally the precipitates was washed with distilled water and dried in hot air oven followed by calcination at 500 °C in the furnace for 5 h [20]. Furthermore, the nickel doped hematite Ni-α-Fe$_2$O$_3$ nanoparticles were synthesized from the same above mentioned procedure with the addition of Ni^{2+} as dopant in calculated quantity [21].

Synthesis of ternary nanocomposite [Pani/Ni-α-Fe$_2$O$_3$/CNT]

In order to prepare the ternary nanocomposite labelled as PNFC, 0.83 M hydrochloric acid aqueous solution was used for dissolving 1 mL of aniline through stirring for 30 min [22].

7

0.05 g MWCNT were added to above mixture which was subjected to 30 min ultrasonication. Afterwards, the homogenous mixture was stirred vigorously for 30 min followed by addition of 0.01 g of hematite nanoparticles (doped or undoped). This mixture was again ultrasonicated for 30 min. This homogeneous mixture was stirred while 0.18g of potassium persulfate (KPS) was added to it as an oxidant. The obtained precipitates were washed with distilled water followed by drying in hot air oven at 80 $^\circ$C.

Characterization

The Scanning electron microscopy (SEM) and energy dispersive X-ray analysis (JEOL JSM-6300) were applied for the morphological study and elemental analysis for which the gold sputtering of the sample was performed prior to analysis. The structural analysis was performed in order to understand the crystal structure by employing the Theta-Theta instrument which used the X-ray radiation beam of Cu Kα (λ = 0.15418 nm) which were accelerated with a voltage of 40 kV and current of 40 mA at room temperature. The Fourier transform Infra Red (FTIR) spectrophotometer (Perkin–Elmer SPECTRUM1000) was employed to acquire the infrared (IR) transmittance spectra at room temperature whereas the instrument has the resolution of 1 cm^{-1} using the KBr matrix as pellets.

Photo electrochemical measurements [PEC]

The photoactive electrodes were exposed to light in a homemade chamber PEC tests. For acquiring the electrochemical data of the respective photoactive electrode, high performance Reference 600+ potentiostat/galvanostat (Gamry Instruments, Warminster, PA, USA) was used in three electrode assembly of the electrochemical cell while Ag/AgCl was used as reference electrode, the counter electrode was a platinum wire whereas the working electrode was based on indium tin oxide (ITO) (1 x 1 cm^2) at room temperature. The Nyquist plot was acquired in the frequency range of 10 Hz to 1 MHz with AC perturbation of 10 mV amplitude in open circuit potential of 0.2 V vs Ag/AgCl as reference electrode using a redox

probe (0.1 M KCl & 2 mM $K_3[Fe(CN)_6]/K_4[Fe(CN)_6]$ in 1:1) solution at pH 7 in dark and illumination. As illumination source, a Xe lamp of 500 W (PL-G500L) (I = 1800 W m^{-2}) with wavelength range of approximately 350–780 nm (Beijing Pulinsaisi) was employed. The capacitance (*C*) of the respective electrodes was measured using the imaginary impedance (Z_{img}) acquired at 100 Hz frequency (*f*) since the semiconductor properties show stability at this frequency while approximation followed was done as;

$$C = -\frac{dQ}{d\psi_o} = \frac{1}{2\pi f |Z_{img}|} \dots\dots\dots\dots\dots\dots\dots\dots (1)$$

Furthermore, the total capacitance (*C*) which having input of both the space charge capacitance ($C_{SC} = dQ_{SC}/d\psi_o$) as well as the double layer capacitance ($C_{dl} = dQ_{dl}/d\psi_o$) that are in series, is therefore used to approximated the C_{SC} by taking C_{dl} of 30 μF cm^{-2} constant value since ψ_o is the Galvanic potential difference;

$$\frac{1}{C} = \frac{1}{C_{dl}} + \frac{1}{C_{SC}} \dots\dots\dots\dots\dots\dots\dots\dots (2)$$

Photocatalytic degradation of Sunset Yellow dye

For evaluating the photocatalytic degradation behavior, 10 mL of the dye was taken in the respective concentration to which 0.01g of the photocatalyst was added. Afterwards, 2 mL H_2O_2 (30% v/v) was added to this reaction mixture as an oxidant followed by subjection to the visible light illumination. Then, the photocatalyst separation was achieved by centrifugation (10,000 rpm for 30 min) (Hettich MIKRO 220) from the reaction mixture and the supernatant absorbance was determined through spectrophotometric analysis by employing a UV/visible double beam spectrophotometer (Hitachi Model U-2500) at 480 nm wavelength, respectively.

Photodegradation kinetic parameters

In order to carry out the kinetics study of photodegradation, the Sunset Yellow dye solution having 2, 6, 10 and 20 ppm concentration was prepared. These respective solutions were photocatalytically degraded with photocatalyst dosage of 0.01 g/10 mL while using 2 mL

H_2O_2 (30% v/v) as oxidant. Then, the absorbance of the supernatant obtained after the centrifugation at regular time intervals was performed using the spectrophotometer (5, 15, 30, 60 and 180 min). Then the concentration of the dye was evaluated using the standard calibration curve in accordance to the Beer Lambert law. After non linearly fitting the acquired kinetic data with the Langmuir-Hinshelwood Model, the different parameters of the kinetic such as the reaction rate constant k_r (mg/L min) and the adsorption constant k_s (L/mg) were determined.

Results & Discussion

Scanning Electron Microscopy (SEM)

As evident in Fig. 1 (a), the SEM micrograph of the undoped α-Fe_2O_3 NPs show uniformity with respect to the morphology. In contrast to the micron-sized agglomerated particles, the size of undoped α-Fe_2O_3 NPs varies from 100 to 150 nm. The large size of the NPs can be corresponded to the Ostwald ripening process which leads to increase in the particle size. Similarly, for Ni-α-Fe_2O_3 NPs as depicted in Fig. 1 (b), the homogeneity is evident with respect to the morphology while the particles diameter lies in the range of 50 to 100 nm. There is a clear decrease in the particle size with the Ni doping which can be attributed to heterogeneous nucleation phenomenon. Also, in contrast to both U-α-Fe_2O_3 NPs, Ni-α-Fe_2O_3 and Pani, the GnP exfoliated flakes are also evident with compact packing in polymer matrix of Pani as shown in Fig.1 (d & e). The ternary nanocomposites of [Pani/Ni-α-Fe_2O_3/CNT] PNFC displayed a heterogeneous morphology with the respective Ni-α-Fe_2O_3 NPs embedded in the Pani matrix as shown in Fig. 1 (c) whereas the MWCNTs were also embedded in the Pani matrix during insitu polymerization process. This indicated the fact that that there is an interaction between the MWCNTs and NPs with the polymer matrix. The different phases seem to have blended evenly in the Pani polymer matrix.
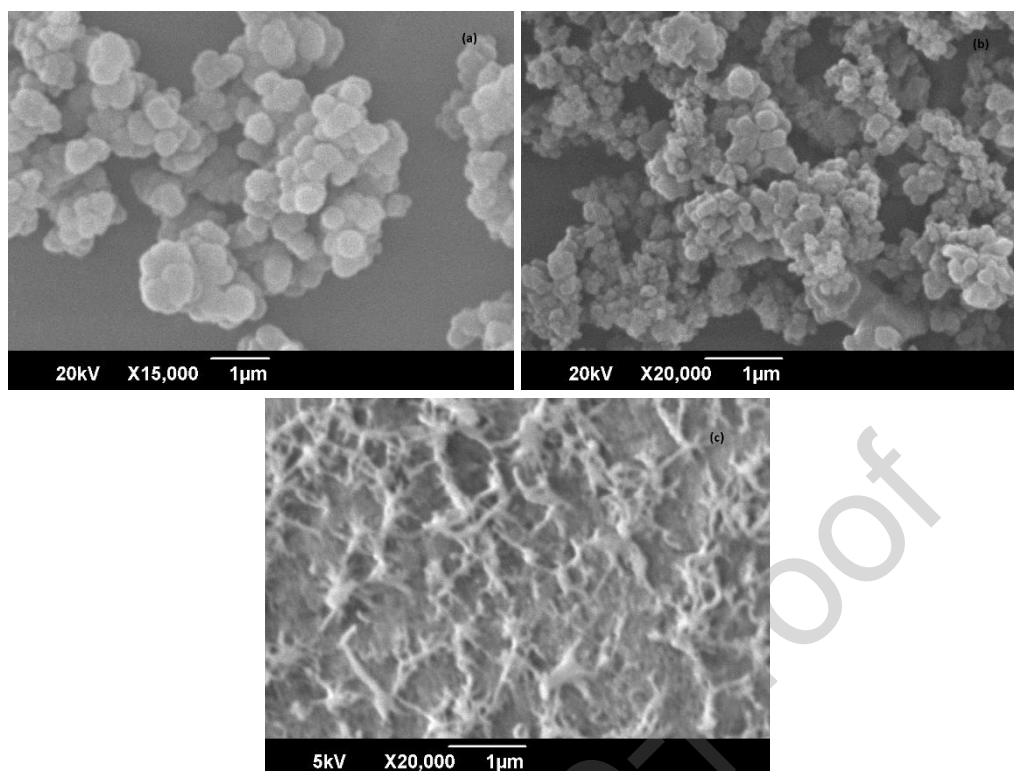
10

Fig. 1 SEM micrographs of (a) α-Fe$_2$O$_3$ NPs,(b) Ni-α-Fe$_2$O$_3$ NPs, and (c) Pani/Ni-α-Fe$_2$O$_3$/CNT ternary nanocomposite (PNFC).

Fourier Transform Infrared Spectroscopy (FTIR)

To further understand the molecular structure of the desired product, FTIR spectroscopy was employed. The fundamental oscillations of the stretching mode assigned to the Fe-O bond appears at 533 cm^{-1} in the IR spectra as shown in Fig. 2 [23, 24]. Accordingly, the oscillations of the asymmetrical mode assigned to the -OH group is at ~3445 cm^{-1}, whereas the bending oscillation associated with the water molecule occurs at around 1633 cm^{-1}, indicating the presence of water molecules adsorbed at the surface of the products. Pani has the benzenoid rings which have characteristic stretching vibrational peaks for the C=C group appears respectively at 1471 cm^{-1}, respectively. The secondary amine has the C-N moiety having the stretching oscillations appearing as IR band at 1279 cm^{-1}, depicting the existence of the intrinsic bipolaron structure in Pani [25]. The peaks associated to the bending oscillations in and out of plane for the C-H moiety present in the 1,4-disubstituted aromatic ring appear at 1065 cm^{-1}, accordingly [26]. The intrinsic double bond oscillations appear as IR peak at 1723

11

cm^{-1} depicting the MWCNTs presence in the ternary nanocomposites [27]. The FT-IR spectra of the respective ternary nanocomposite samples as shown in Fig. 2 (a, b & c) has the sharp and prominent peaks for the vibrational bands of α-Fe$_2$O$_3$ in addition to the respective red shifts pointing to the interaction of electronic nature between Pani, MWCNTs and α-Fe$_2$O$_3$ phase [28]. Therefore, these results of FTIR spectroscopy confirm the successful embedment of the α-Fe$_2$O$_3$ in the Pani matrix since the appearance of the intrinsic IR peaks confirms the ternary nanocomposite formation.

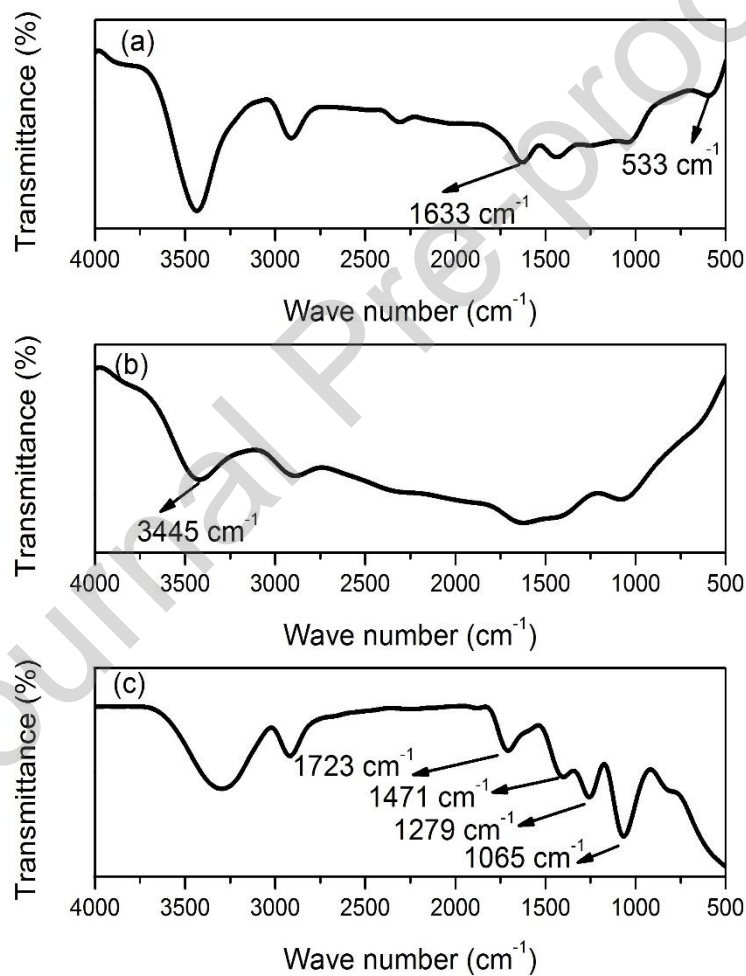Fig. 2 FTIR spectrum of (a) α-Fe$_2$O$_3$ NPs,(b) Ni-α-Fe$_2$O$_3$ NPs, and (c) Pani/Ni-α-Fe$_2$O$_3$/CNT ternary nanocomposite (PNFC).

X-ray Diffraction (XRD)

The crystalline assembly of the respective samples was determined using XRD analysis. The reflections for the (012), (104), (110), (113), and (024) crystal planes of the

12

respective trigonal crystal system are found at $2\theta = 23.95^\circ$, 33.20°, 35.50°, 43.89° and 49.25° in the XRD pattern for the α-Fe_2O_3 and Ni-α-Fe_2O_3NPs, as shown in Fig. 3 (a-b) [29]. The α-Fe_2O_3 and Ni-α-Fe_2O_3NPs exhibit good crystallinity and purity as evident by the narrowness and sharpness of the peaks. The respective peaks for the α-Fe_2O_3 and Ni-α-Fe_2O_3NPs also appear in XRD patterns for the PNFC ternary nanocomposite as they are embedded in the polymer matrix as shown in Fig. 3 (c). Similar the X-ray diffraction analysis also affirms the Pani in PNFC with the orthorhombic structure having the orthorhombic space group P_{bcn} whose reflections are located at $2\theta = 19.25^\circ$, 28.8°, and 31.35° pertaining to the respective crystal plane of (110), (200), & (211) [30]. Additionally, the quinoid and benzenoid rings are arranged in a regular way that is evident with a peak at $2\theta = 25.5^\circ$ depicting the phenyl rings interlayer spacing for the stacks of the neighbouring chains in parallel planes. These results affirm the semi-crystalline nature of the Pani [31]. Furthermore, the stacks of graphitic carbon hexagonal layers has the reflection appearing at 26.48° corresponding to the (002) plane confirming the presence of MWCNTs embedded in the polymer matrix. The XRD patterns don't have the peaks for Ni or NiO which was indicative of good crystallinity and high purity of the doped samples. Moreover, with the Ni doping, the respective peaks for the α-Fe_2O_3 show an increase in intensity as well as in peak width depicting the decrease in crystallite size as confirmed by Scherrer formula. There is also slight shift in the peaks for α-Fe_2O_3 structure in addition to change in the full width half maximum value when doped with Ni which established the Ni integration into the α-Fe_2O_3 lattice [32]. The interlayer spacing was determined using the Bragg's equation given as;

$$2d_{hkl}\, sin\theta_{hkl} = n\lambda \;..\; (3)$$

whereas d_{hkl} denotes the interlayer spacing, θ_{hkl} represents the peak location as the angle of incidence, λ is the respective mean $Cu\ K_{\alpha 1}$ wavelength and n is the order of diffraction (n =

13

1, 2, ...). The crystallite size (*D*) was determined using the Debye-Scherer's formula for the respective samples;

$$D = \frac{K\lambda}{\beta \cos \theta_{hkl}}$$ .... (4)

whereas *D* represents the crystallite size, *K* = 0.89 as the shape parameter, λ = 0.154056 nm is the mean *CuK$_{\alpha 1}$* radiation wavelength while *β* is the full-width-half-maximum (FWHM) value of the corresponding reflections at the Bragg's angle *θ* (rad) and converted into angle from radian for analysis. The FWHM was determined using the origin software while employing the gaussian function. The evaluated values of the structural parameters for the respective samples are listed in Table 1. As iron Fe (III) has 6 coordination number in α-Fe$_2$O$_3$ structure since the oxygen ions are in hcp arrays of the Hematite's structure along the [001] direction in which Fe (III) ions occupy two thirds sites trailed by one vacant site in the respective (001) plane. In addition, Ni has the coordination number of 6 as well for Ni^{2+} having octahedral symmetry with the O^{2-} ligand due to which it fits very well in the FeO$_6$ octahedra in α-Fe$_2$O$_3$ structure [33].

Table 1

Evaluation of crystallite size of the as prepared samples

Samples	K	λ (nm)	β (rad)	θ$_{hkl}$	D (nm)
α-Fe$_2$O$_3$ NPs	0.89	0.154	0.00415	21.95	31.37
Ni-α-Fe$_2$O$_3$ NPs	0.89	0.154	0.00716	21.95	15.58
Pani/Ni-α-Fe$_2$O$_3$/CNT	0.89	0.154	0.01050	21.95	11.71
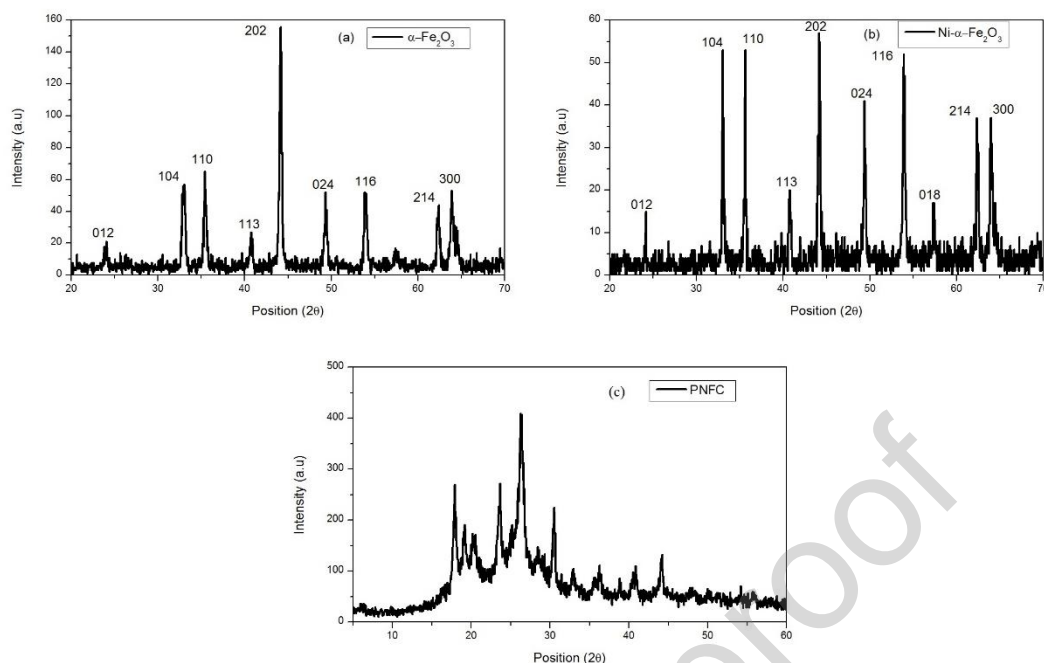
Fig. 3 XRD spectrum of (a) α-Fe$_2$O$_3$ NPs, (b) Ni-α-Fe$_2$O$_3$ NPs, and (c) Pani/Ni-α-Fe$_2$O$_3$/CNT [PNFC] ternary nanocomposite.

Energy Dispersive X-ray analysis

The elemental analysis was performed using the EDX in order to confirm the presence of the respective elements in the as prepared sample which is displayed in Fig. 4 (a-c) for α-Fe$_2$O$_3$ NPs, Ni-α-Fe$_2$O$_3$ NPs, and Pani/Ni-α-Fe$_2$O$_3$/CNT [PNFC]. Furthermore, the respective percentage composition of the each element is also listed in Table 2. The peaks at 6.398 keV and 0.525 keV for Fe (K$_\alpha$) and O (K$_\alpha$) confirm the presence of the iron and oxygen in the samples of the α-Fe$_2$O$_3$ and Ni-α-Fe$_2$O$_3$ NPs and the respective PNFC ternary nanocomposites. However, for Ni incase of Ni doped α-Fe$_2$O$_3$, the Ni (K$_\alpha$) maxima appears at 7.480 keV validates the Ni presence in the samples containing Ni-α-Fe$_2$O$_3$ NPs. Likewise, the presence of carbon [C(K$_\alpha$)], nitrogen [N(K$_\alpha$)] & chlorine [Cl(K$_\alpha$)] in Pani is affirmed by the presence of the peaks at 0.277 keV, 0.392 keV and 2.621 keV in case of the nanocomposites (ternary) containing the polymer matrix of Pani, respectively. The extra maxima that appears in Fig.4 (a-c) corresponding to the silicon (1.740K$_\alpha$), sodium (1.040K$_\alpha$), & chloride (2.621K$_\alpha$) are attributed to the glassy substrate employed for the performing the EDX/SEM.
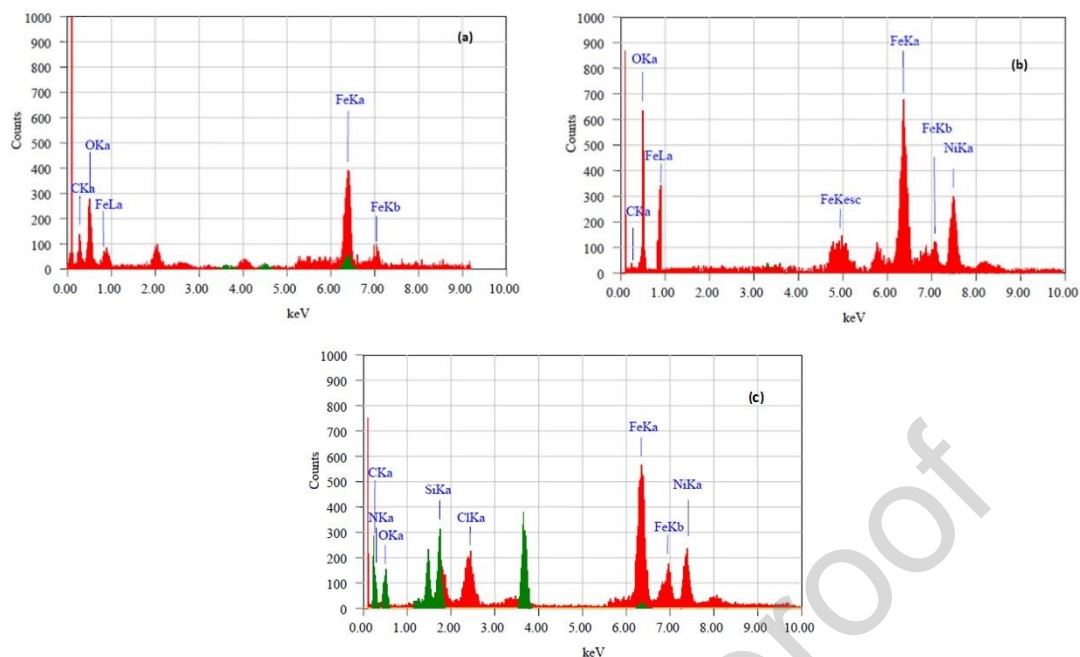
15

Fig. 4 EDX spectrum of (a) α-Fe₂O₃ NPs,(b) Ni-α-Fe₂O₃ NPs, and (c) Pani/Ni-α-Fe₂O₃/CNT [PNFC] ternary nanocomposite.

Table 2
EDX elemental composition for quantitative analysis

α-Fe₂O₃ NPs		
Element	**(keV)**	**Mass%**
C K_α	0.277	4.28
O K_α	0.525	23.50
Fe K_α	6.398	72.22
Total		**100.00**
Ni-α-Fe₂O₃ NPs		
Element	**(keV)**	**Mass%**
C K_α	0.277	5.45
O K_α	0.525	23.24
Ni K_α	7.480	5.57
Fe K_α	6.398	65.74
Total		**100.00**
Pani/Ni-α-Fe₂O₃/CNT [PNFC]		
Element	**(keV)**	**Mass%**
C K_α	0.277	14.41
O K_α	0.525	20.30
N K_α	0.392	9.86
Cl K_α	2.622	3.89
Ni K_α	7.480	9.99
Fe K_α	6.398	41.05
Total		**100.00**

Optical Properties

Fig. 5 (A) shows the UV visible spectra of undoped and Ni doped α-Fe$_2$O$_3$ NPs, and the respective PNEC ternary nanocomposite. The α-Fe$_2$O$_3$ NPs depict an energy band gap E_g of 1.76 eV which is validated by Tauc plot analysis since it is in agreement with the maximum absorbance for the α-Fe$_2$O$_3$ NPs occurring at about ~525 nm. This peak at ~525 nm corresponds to the process of the double exciton transitions based on pairs of Fe^{3+} - Fe^{3+} cations as compared to the ligand field transition of the single Fe^{3+} cation [34]. Incase of the α-Fe$_2$O$_3$ NPs, the optical energy band gap is dependent on the existence of cationic or anionic unoccupied sites, states due to structural defects, and interstitials that occur adjacent to the level of the energy band gap [35]. Similarly, the UV-Visible absorbance for the Ni-α-Fe$_2$O$_3$ NPs also lies in the visible range with the maximum absorbance occurring at ~540 nm. This apparent redshift points to the decrease in the energy of the optical band gap [36]. In the instance of the respective ternary nanocomposites, a red shift takes place when the maximum absorbance occurs in the range of ~600 to ~750 nm, showing an improvement in the utilization of visible light energy as a result of band gap extension to the visible region. It can be attributed to the presence of Pani for which the quinoid rings polaron- π^* transition appears at 525 nm whereas the π-polaron transitions (exciton) occur as a peak at 675 nm [7].

The optical band gap (E_g) was calculated using a Tauc plot analysis, which is obtained by plotting ($\alpha h v$)^2 against ($h v$), as shown in Fig. 5 (B). Since the following expression is followed in which the plot linear region is extrapolated to $\alpha = 0$ [37];

$$\alpha = A(h v - E_g)^n \quad .... (5)$$

while $h v$ denotes the photon energy, α is the absorption coefficient whereas the edge parameter is represented A. The value of $n = \frac{1}{2}$ for direct transitions in the case of α-Fe$_2$O$_3$, Ni-α-Fe$_2$O$_3$ NPs, and the ternary nanocomposite PNFC. Accordingly, the optical band gap (E_g) values which are calculated are listed in the Table 3 which clearly show decrease in the optical

17

band gap pertaining to the photosensitization of the Ni-α-Fe$_2$O$_3$ NPs through functionalization with Pani. The induced strain or size effect (Bohr exciton radius) due to doping are associated with the decrease in E_g due to the apparent red shift [38]. As the induced strain induces the crystal defects in α-Fe$_2$O$_3$ structure, the redistribution of the band to tail energy levels thus takes place allowing the transition from tail to tail and band to tail which leads to the band shrinkage [39]. Since, the graphitic layers in MWCNTs has been decorated with hematite nanoparticles on its surface, Fe^{2+} in the α-Fe$_2$O$_3$ structure interacts with the oxygen-containing carbon moieties on the MWCNTs leads to the production of electron-hole pairs. Also, the transition of electrons of the π-π^*, π^*-polaron, and π-polaron nature in Pani renders the ternary nanocomposites to absorb to considerable extent in the UV and visible region. Furthermore, the new excitation processes occur due to the addition of MWCNTs, since they can be ascribed to the graphene sheets sp^2 clusters, indicating the appearance of the quantum confinement [40]. The ternary nanocomposite will therefore, generate the most electron-hole pairs as a consequence, which will validate the occurrence of the photosensitization phenomenon. By using Polyaniline (Pani) to sensitize α-Fe$_2$O$_3$ structure as an n-type semiconductor, the visible spectrum at longer wavelengths may be used more effectively. An electron is subsequently transferred to the α-Fe$_2$O$_3$ conduction band by the oxidation of the excited Pani present at the semiconductor surface. However, the hole produced in the valence band of the semiconductor without sensitization is at a more positive potential than the one produced by the electron transfer to the semiconductor conduction band by light. Furthermore, E_g reduction with Ni doping can also be attributed to increase in charge carrier density.

The calculation of the Urbach energy obtained from Urbach plot as shown in Fig. 5 (C) provides additional evidence for the decrement in the band gap (optical) energy E_g of the ternary composite in comparison to the α-Fe$_2$O$_3$ and Ni-α-Fe$_2$O$_3$ NPs. The improvement occurs when there is a decline in the decrementing energy transitions since the addition of the Ni-α-

Fe$_2$O$_3$ NPs to the Pani matrix, leads to the creation of the band gap level defects that are potential electron trap sites. As these electron traps are confined levels which are introduced into the band tails known as the Urbach tails. Furthermore, their respective energy as the Urbach energy associated with the defect-tail width as it is the width of the localized charge carrier trap sites tail in the band gap region. The Urbach energy of the respective ternary nanocomposite as listed in Table 3 is more in comparison to α-Fe$_2$O$_3$ and Ni-α-Fe$_2$O$_3$ NPs. This difference can be attributed to the ternary nanocomposite PNFC structural and morphological modifications. Similar to this, the widening of the localized trap sites that are introduced into the band gap, which is apparent as the increase in the Urbach energy due to the sensitization, can be associated to the reduction in optical band gap energy E_g [41].

In the vicinity of the lower photon energy region, the absorption coefficient α exhibits an exponential relationship known as the Urbach empirical rule, which is expressed mathematically as [42];

$$\alpha = \alpha_o \exp\left(\frac{hv}{E_u}\right) \quad\text{................................ (6)}$$

whereas hv denotes the energy of photon, α_o designates a constant, and E_u indicates the Urbach energy. The Urbach energy, E_u, explains the width of the exponential absorption edge acquired from the Urbach plot slope according to the following relation as;

$$E_u = \left[\frac{d(\ln \alpha)}{d(hv)}\right]^{-1} \quad\text{................................ (7)}$$

Table 3

Optical band gap energy (E_g) and Urbach Energy (E_u) for the respective samples

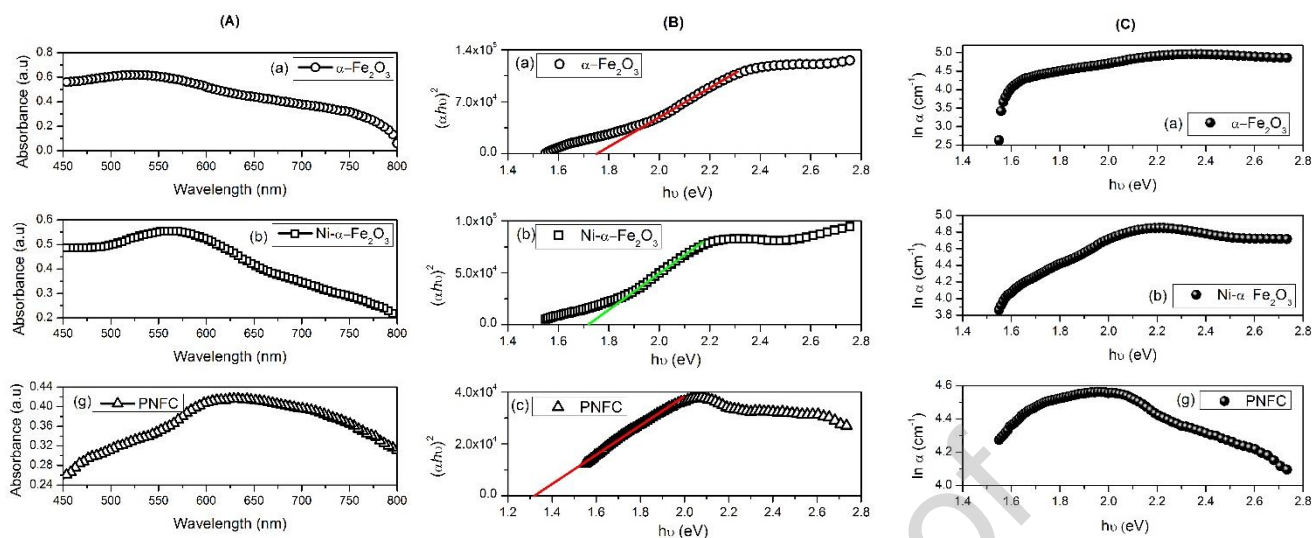|	α-Fe$_2$O$_3$ NPs	Ni-α-Fe$_2$O$_3$ NPs	Pani/Ni-α-Fe$_2$O$_3$/CNT [PNFC]
E_g (eV)	1.76	1.72	1.32
E_u (eV)	1.33	1.55	0.72

Fig. 5 UV-visible absorbance spectra (A), a Tauc plot (B), and an Urbach plot (C).
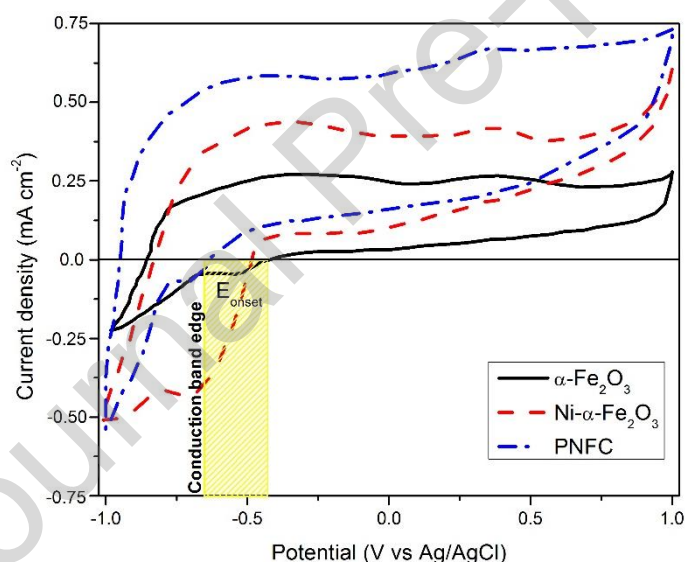
Photo-electrochemical Measurements

Fig. 6 Cyclic voltammogram acquired in dark using 0.1 M NaOH as supporting electrolyte at 30 mV s^{-1} scan rate.

Cyclic voltammetric measurement across -1.0 to 1.0 V potential range were acquired in the dark using 0.1 M NaOH as the electrolyte while employing Ag/AgCl as reference electrode. The conduction band edge as depicted by the onset potential value (E_{onset}), was determined approximately by extrapolating the current density value to zero at point where the cathodic current trace begins to appear as shown in Fig. 6. Hence, the onset potential value

20

(E_{onset}) locates the position for electron accumulation at the bottom of conduction band. Incase of α-Fe$_2$O$_3$ electrode, the onset potential (E_{onset}) value is -0.457 V whereas -0.492 V and -0.638 V is acquired for Ni-α-Fe$_2$O$_3$ and PNFC based electrodes, respectively. As apparent, there is cathodic shift in the E_{onset} values of Ni-α-Fe$_2$O$_3$ and PNFC which is remarkable. This enhancement is probably due to reduction the surface electron hole recombination due to Ni doping and surface modification with Pani [43]. Another suggestion for the band level positioning in Ni-α-Fe$_2$O$_3$ and PNFC is the occurrence of the shallow donors due to doping in comparison to the deep electron traps in pure α-Fe$_2$O$_3$ [44, 45]. Also the accelerated hole transfer across the semiconductor-electrolyte can be attributed to the suppression of recombination processes [46]. Therefore, the cyclic voltammetric studies demonstrate that both the dopants and surface modification with Pani complement each other in improving the current density and reducing the onset potential. The quasi-rectangular shape of the cyclic voltammograms owes to the reversible redox reactions of the Fe^{3+} and Fe^{2+} ions in the NaOH electrolyte which intercalates with the electrode material [47].
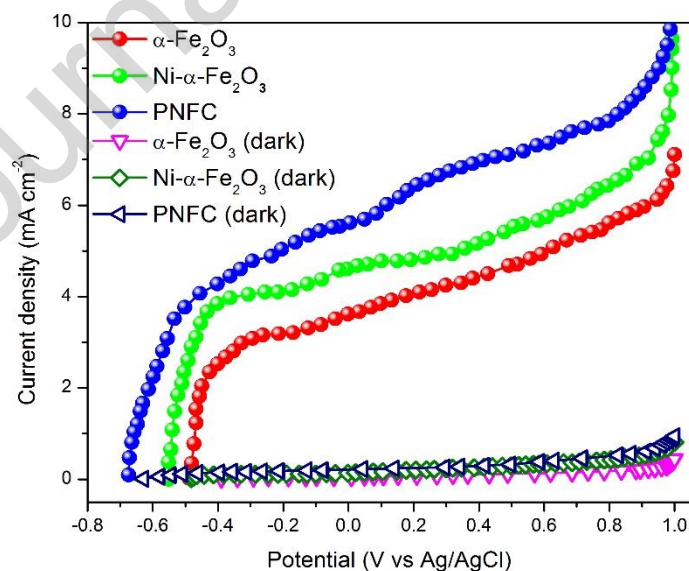

Fig. 7 J-V characteristics recorded in a three-electrode cell using Pt as counter electrode, Ag/AgCl as reference electrode, and 1 M NaOH as supporting electrolyte. Xenon lamp with power density of 1800 mW m^{-2} was used as light source for the excitation.

The surface modification of Ni-α-Fe$_2$O$_3$ with Pani indeed shifts the Fermi level to more negative potential while improving the photo electrochemistry of the ternary composite PNFC. For the evaluation of this influence on energetics, the electrodes based on α-Fe$_2$O$_3$, Ni-α-Fe$_2$O$_3$ and PNFC were employed as photoanode using 1 M NaOH as supporting electrolyte in a photoelectrochemical cell. The acquired J-V characteristics are displayed in Fig. 7. Apparently the potential at which the current density is zero corresponds to the flat band potential since the net current flow reduces to zero at this applied potential due to recombination of all the photogenerated electrons and holes. Also, the negative bias which is applied counter balances any built-in driving force for transporting electrons to the electrode-electrolyte interface [48]. Therefore, the zero-current potential value can be adopted to evaluate the flat band potential (or apparent Fermi level) of the as prepared samples. As depicted in Fig. 7 that the apparent value of the flat band potential for α-Fe$_2$O$_3$, Ni-α-Fe$_2$O$_3$ and PNFC in 1M NaOH is at -0.49 V, -0.55 V and -0.68 V vs Ag/AgCl. The flat band potential shows a significant shift to the negative potentials for the ternary nanocomposite PNFC, respectively. This fact is visible as significant photocurrent trace for PNFC at -0.60 V vs Ag/AgCl potential whereas on the other hand, absolute recombination is observed in pristine α-Fe$_2$O$_3$. Obviously, the surface modification in addition to doping of α-Fe$_2$O$_3$ facilitates the electron-hole pair separation and accelerates the electron transfer at the electrode-electrolyte interface. Therefore an enhancement is observed in the photoelectrochemical behavior as reflected in the generated photocurrent. The traces of the photocurrents are significantly higher at positive bias. The photocurrent of 4.52 mA cm^{-2} is observed for the pristine α-Fe$_2$O$_3$ whereas 7.04 mA cm^{-2} is recorded for the ternary composite PNFC at 0.4 V vs Ag/AgCl. The appreciable enhancement of the photoelectrochemical behavior appears as increment in the photocurrent density. Barber et al. reported that the doping of the α-Fe$_2$O$_3$ nanorods with 5 mol% Mn enhanced the photocurrent densities by 3 times at 1.23 V vs. RHE as compared to pristine hematite. In

addition, the surface treatment of the spray pyrolyzed hematite mesoporous thin films with ZnAc also resulted in enhanced PEC performance apparent as more than 40% increase to 1.08 mA cm^{-2} at 0.23 V vs. Ag/AgCl [46]. Zhong and co-workers also recorded an increase in the photocurrent density form 0.87 mA/cm^{-2} at 1.23 V vs. RHE for the pristine α-Fe$_2$O$_3$ to 1.61 mA/cm^{-2} for the optimized Ti-modified hematite [45]. Doping process also results an improvement in the PEC response according to Pan et al. which was exhibited as $\sim$6 folds increase in the photocurrent density at 0 V versus Ag/AgCl ($\sim$1.0 V vs RHE) for the 3% Au-modified hematite thin film [49]. In case of our study, however, the exploitation of the visible region of the electromagnetic spectrum enable the ternary nanocomposite PNFC to hinder the photo generated electron hole pair recombination under irradiation. Hence a considerable photocurrent flow is observed as depicted in Fig. 7 when more positive bias is employed as compared to the flat band potential (E_{fb}). The photogenerated holes in the space-charge region are accelerated to the semiconductor-solution interface leading to the oxidation at electrode potential which is effective with respect to the valence band edge energy level. Contrary to this, the excess electrons are accelerated towards the bulk region under applied electric field and hence contribute to the photoanodic current density due to ease in electron mobility in the ternary nanocomposite PNFC [50].
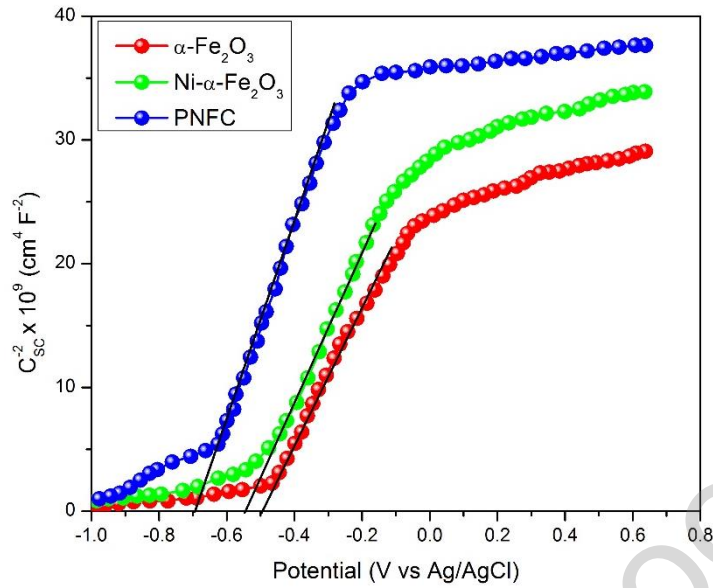
Fig. 8 Mott–Schottky (M–S) plots ($1/C^2$ vs. V) of α-Fe$_2$O$_3$, Ni-α-Fe$_2$O$_3$ and PNFC electrodes immersed in 0.1 M NaOH as supporting electrolyte.

The flat band potential (E_{fb}) corresponding apparently to the Fermi level of the semi-conductor was determined from the Mott-Schottky analysis. The space charge capacitance C_{sc}^{-2} was plotted against the applied potential E to acquire the Mott-Schottky plot as displayed in Fig. 8 [51]. An AC perturbation of $\pm$ 10 mV at 1 kHz frequency having 30 mVs^{-1} scan rate was employed in order to obtain the space charge capacitance C_{sc}^{-2} in the potential range of -1.0 to 0.7 V vs Ag/AgCl as reference electrode using 0.1 M NaOH as supporting electrolyte under illumination. The linear behavior of C_{sc}^{-2} against the applied potential with positive slope is indicative of n-type semi-conductivity in α-Fe$_2$O$_3$, Ni-α-Fe$_2$O$_3$ and ternary nanocomposite PNFC. Since, the doping of α-Fe$_2$O$_3$ with nickel result in interstitials defects or oxygen vacancies (V$_o$) which promote the free electrons transport to conduction band [52]. In order to evaluate the flat band potential (E_{fb}) as well as the donor densities (N_d), Mott-Schottky expression is applied [53];

$$\frac{1}{C_{sc}^2} = \frac{2N_A}{N_d F \varepsilon_r \varepsilon_o}\left[E_m - E_{fb} - \frac{RT}{F}\right] \quad \text{...........................} (8)$$

24

whereas N_A denotes the Avogadro's number (6.022×10^{23} mol^{-1}), N_d (cm^{-3}) depicts the donors density, F denotes the Faraday's constant ($\sim 9.65 \times 10^4$ C mol^{-1}), ε_r is the dielectric permittivity, ε_o is the free space permittivity ε_o (8.8542×10^{-14} F cm^{-1}), E_m (V) represents the applied potential for C_{sc}^{-2} measurement, E_{fb} denotes the flat band potential, R denotes the ideal gas constant (8.314 J K^{-1} mol^{-1}), and T is the absolute temperature ($\sim$ 298 K). Also, the donor concentrations (N_d) is attained from the linear region slope $[d(C^{-2})/dE]$ of the Mott-Schottky plot in accordance with the following expression [54];

$$N_d = \frac{2N_A}{F\varepsilon_r\varepsilon_o}\left[\frac{dE}{d(C^{-2})}\right] \quad .... (9)$$

The donor concentration (N_d) for the α-Fe$_2$O$_3$, Ni-α-Fe$_2$O$_3$ and ternary nanocomposite PNFC is 4.83 x 10^9, 5.77 x 10^9 and 7.68 x 10^9 cm^{-3}, respectively. As evident, the N_d value increase for the ternary nanocomposite PNFC points to the proximity of the Fermi (E_f) level below the CB edge [55]. Hence, the improvement of the charge transfer rate due to increase in its donor concentration N_d leads to an enhanced PEC activity.

As an important parameter of semiconducting material, the flat band potential (E_{fb}) reflects the Fermi level position before establishing interface with the electrolyte. As the surface electron depletion occurs at semi-conductor/electrolyte interface due to applied voltage perturbation, the band bending takes place which will also be affected by the separation of the Fermi levels of semiconductor and redox specie under the influence of the applied voltage change [56]. However, when the band bending disappears, then the applied voltage corresponds to the flat band potential (E_{fb}). The flat band potential (E_{fb}) values obtained for α-Fe$_2$O$_3$, Ni-α-Fe$_2$O$_3$ and the ternary nanocomposite PNFC are -0.493, -0.556 and -0.692 V vs Ag/AgCl in accordance with the intercept of the Mott-Schottky plot acquired after the extrapolation of linear region to $1/C^{-2} = 0$ that is equivalent to $E_{fb} + (RT/F)$, respectively. With regards to these results, it can be suggested that the photogenerated delocalized electrons are rapidly

promoted to the vacant CB level. Therefore, the photo-excited charge carrier (e⁻ - h⁺) pairs are spatially separated which also accelerated the transfer of holes to VB since they are trapped by the crystal lattice defect sites due to doping [57]. Also, the cathodic shift of the flat band potential (E_{fb}) results in Fermi (E_f) level positioning more close to negative potentials i-e increased band banding (E_b) given by $E_m - E_{fb}$ leading to increased charge carrier separation [58-60]. For the anodic potentials as compared to the flat band potential (E_{fb}), an electric field establishes due to depletion of charge carriers. The affect of aforementioned phenomenon on an n-type semi-conductor PEC enhancement then even appears at low potential due to more negative flat band potential (E_{fb}) [7]. Here it can be mentioned that since the crystal structure defect sites shifts the Fermi (E_f) level due to doping. The Fermi level (E_f) shifting develops the surface states due to the localized atomic orbitals energy levels at defect site proximity which relocates the band edges [61].
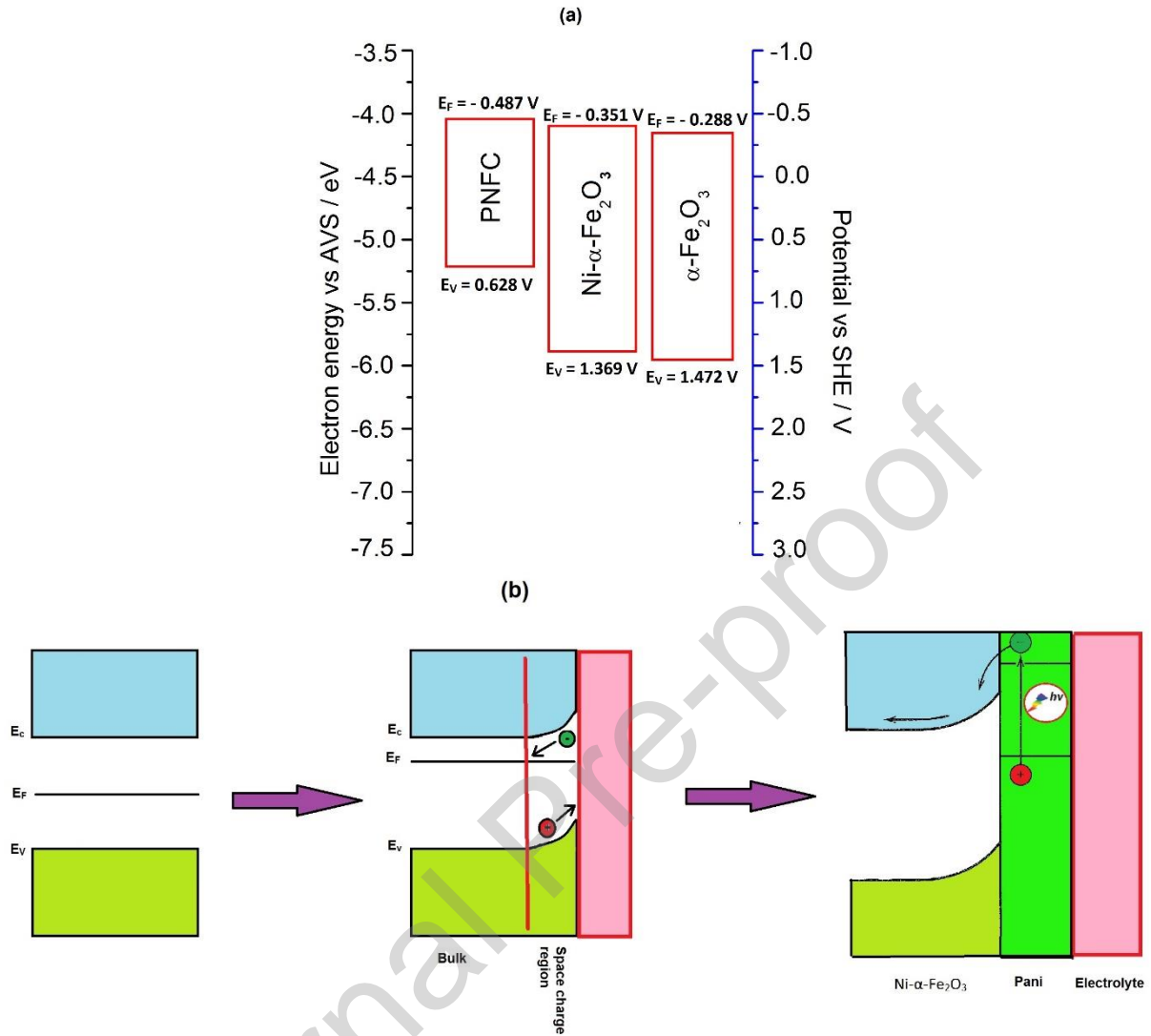
Fig. 9 (a) Electrochemical (V vs. SHE) and potential energy (eV) diagram depicting the position of fermi level (E_F) and valence band edge (E_V). At pH 6 while employing 0.1 M NaOH as supporting electrolyte, E_{fb} (MS) was used for E_F approximation whereas E_V was estimated by summation of E_g to E_F and (b) Illustration depicting the energy level positions.

For energy structure estimation, the position of fermi level (E_F) and valence band edge (E_V) are approximated as displayed in Fig. 9 (a & b). Since the lower end of the conduction band is populated with donor states, the flat band potential (E_{fb}) is then positioned beneath it which is also suggested by the moderate level ($N_d \approx 10^9$ cm^{-3}) of donor concentration. Correspondingly, the Fermi level (E_f) is also located below the conduction band edge by the surface states in n-type semiconductor. The high value of E_F for the ternary nanocomposite PNFC will allow efficient electron flow to the semi-conductor/electrolyte interface due to

which a depletion region is established that hinders electron hole pair recombination. However, the holes have low oxidizing ability since the E_v is less positive for PNFC as depicted shown in Fig. 9 [62].
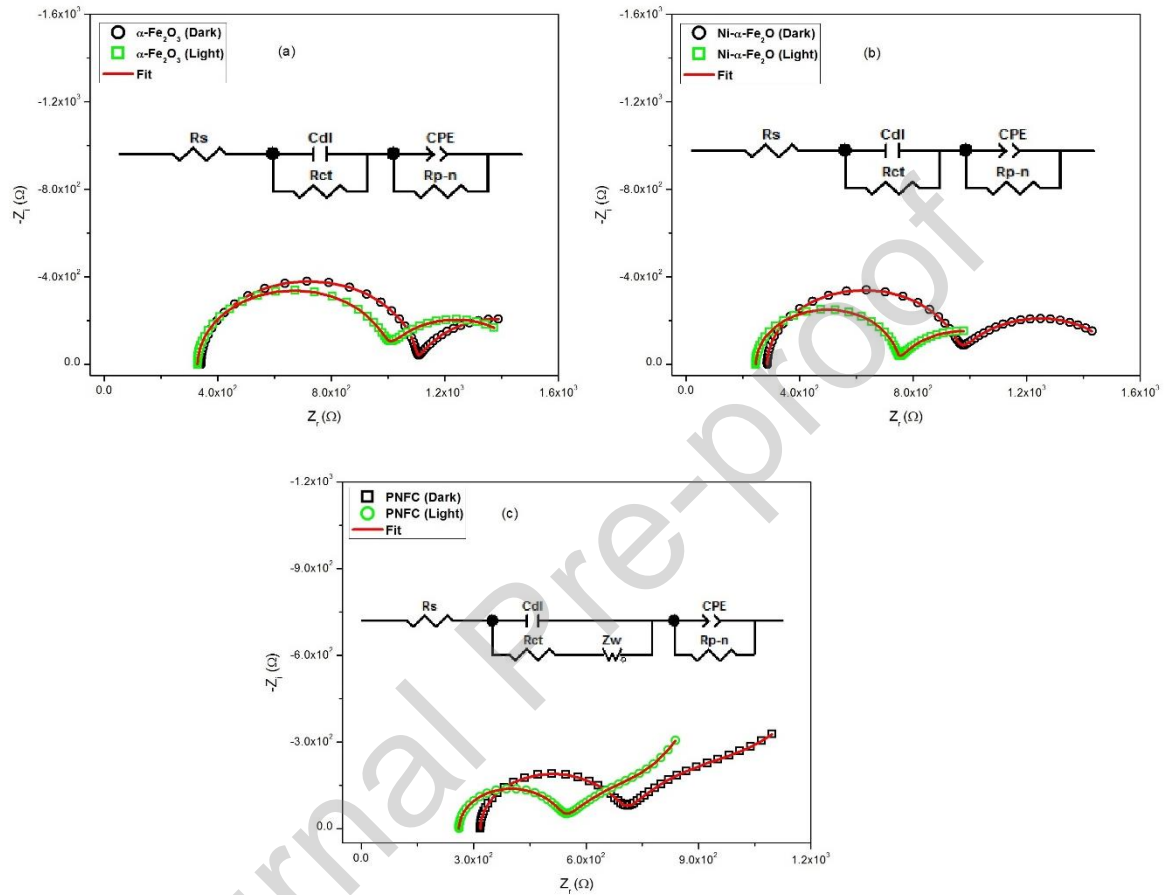

Fig. 10 EIS Nyquist plot with inset showing respective equivalent circuit diagram

Electrochemical impedance spectroscopy (EIS) was employed for understanding the photo-electrochemical response as interfacial charge transfer occurred at the electrode/electrolyte junction. EIS data was recorded under illumination of 100 mW cm^2 as well as in dark from 10 Hz – 1 MHz. Fig. 10 (a, b & c) shows the Nyquist plot for α-Fe$_2$O$_3$, Ni-α-Fe$_2$O$_3$ and the ternary nanocomposite PNFC with the inset depicting their respective equivalent circuit diagrams. The net value of the series resistance including the electrolyte resistance is depicted as R_s in the equivalent circuit diagram. The electrochemical double layer capacitance of the Helmholtz layer at electrode/electrolyte interface is represented as C_{dl}

28

whereas R_{ct} is the interfacial charge transfer resistance for the semiconductor depletion zone depicted by one complete semicircle at high frequency as evident in Nyquist plot. However, the electrochemical double layer offers R_P as the interfacial polarization resistance at the electrode/electrolyte interface visible as a semicircle arc at the low frequency end which decreases upon illumination due to swift charge transfer [63]. Similarly, *CPE* is the constant phase element assigned to the capacitance due to the semiconductor depletion region since the system is non homogeneous and also the charge carriers are diffusing through the electrode. For the R_{ct} values as listed in Table 4 obtained after fitting EIS data with equivalent circuit model, there is notable decrease in its value under illumination whereas R_{dl} which occurs at the semiconductor-solution phase junction decreases with illumination of white light [64]. For the ternary nanocomposite PNFC, R_p value decreases in light as compared to dark depicted as smaller semi-circle arc at low frequency end suggesting the occurrence of the faradaic reaction across the interfacial electrochemical double layer [65]. Since, the GnP as zero band gap material have the $\pi -$ conjugated system which assists the swift transfer of the photo-excited electrons from the α-Fe$_2$O$_3$ NPs conduction band and the LUMO energy level of Pani to the specie in the solution phase [66]. Also the Pani HOMO accommodates the holes transferred to it form the α-Fe$_2$O$_3$ NPs valence band. The π-conjugated system in both the GnP and Pani overlaps which not only facilitates electron transfer but also limits the electron hole pair recombination [67].

Table 4
Values obtained for different elements after EIS fitting for the proposed equivalent circuit.

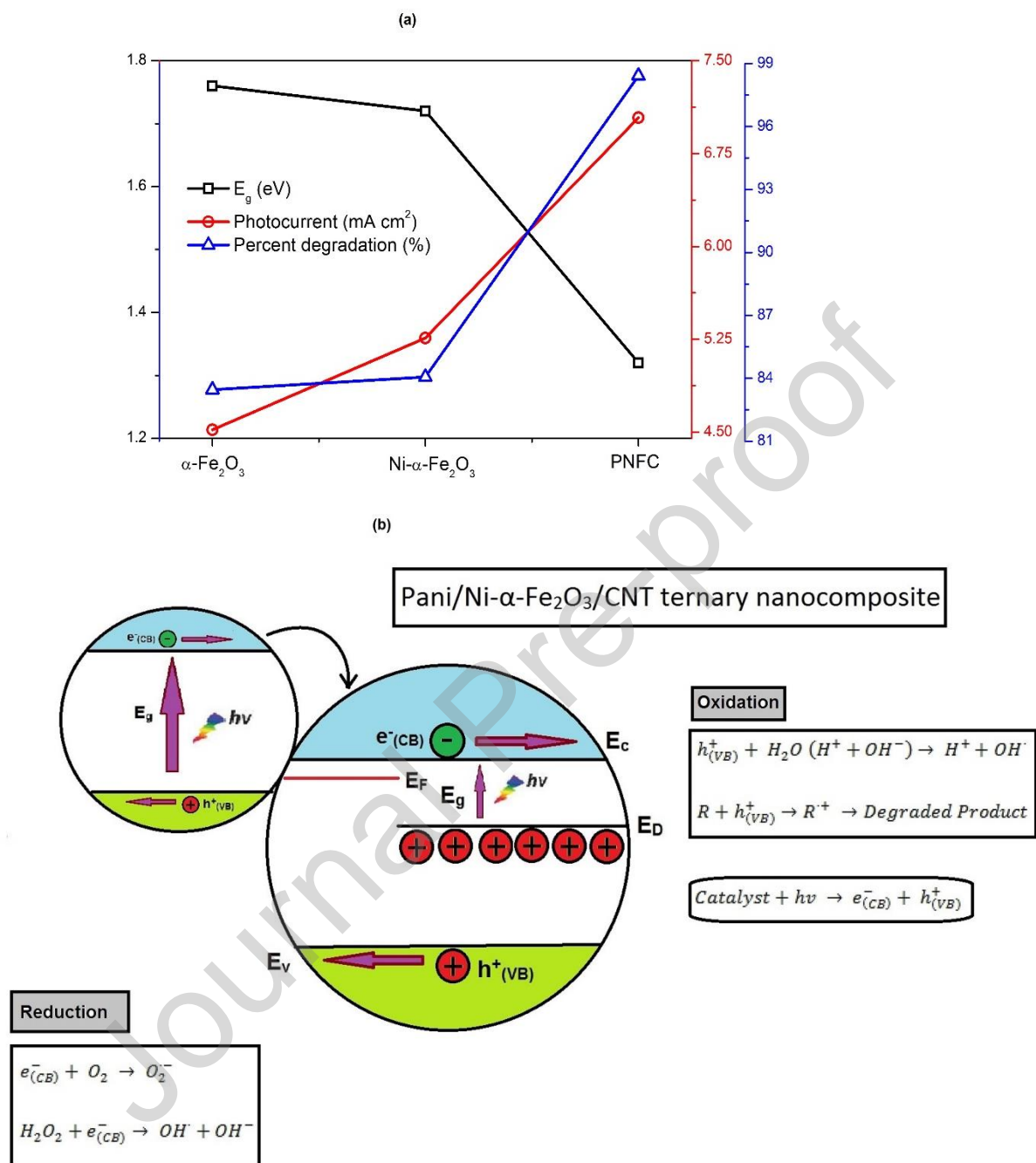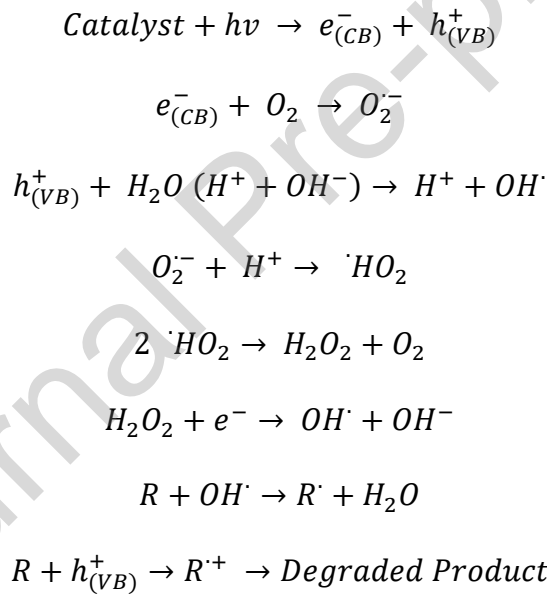|	R_s x 10^2 (Ω)	C_{dl} x 10^{-4} (F)	R_{ct} x 10^2 (Ω)	Z_w-R	Z_w-T	Z_w-P	CPE-T x 10^{-2} (F)	CPE-P (α)	Rp-n x 10^2 (Ω)
α-Fe$_2$O$_3$ (Dark)	3.41	1.0	7.58	0.0949	0.79	582			
α-Fe$_2$O$_3$ (Light)	3.29	7.0	6.64	0.0772	0.86	501			
Ni-α-Fe$_2$O$_3$ (Dark)	2.86	2.0	6.68	0.0336	0.78	592			
Ni-α-Fe$_2$O$_3$ (Light)	2.46	2.0	4.97	0.0857	0.73	471			
PNFC (Dark)	3.18	5.4	3.58	84	29	0.35	6.72	0.82	3.19
PNFC (Light)	2.61	3.6	2.64	73	32	0.4	5.82	0.76	2.47

Investigation of Photo-activity

Fig. 11 (a) Co-relation of the E_g and Photocurrent with the photocatalytic degradation of sunset yellow dye for evaluation of the photo-activity and (b) Illustration depicting the reaction mechanism with respect to the energy level positions

For evaluating the photo-activity of α-Fe$_2$O$_3$, Ni-α-Fe$_2$O$_3$ and the ternary nanocomposite PNFC, the degradation of sunset yellow dye was carried out under visible light irradiation. As evident in Fig. 11 (a & b), the ternary nanocomposite PNFC displayed higher photodegradation efficiency as compared to α-Fe$_2$O$_3$ and Ni-α-Fe$_2$O$_3$. Indeed, the ternary

30

nanocomposite PNFC with lower E_g value and higher photocurrent show higher photo-activity, hence the optical band gap is the principal factor determining the photo-activity. The sensitization of Ni-α-Fe$_2$O$_3$ with Pani is an approach for utilization of longer wavelength light. After excitation, Pani injects a photo-electron into the conduction band of Ni-α-Fe$_2$O$_3$ while itself being oxidized. It's a known fact that the photoelectrochemical cells are created at the surface of the photocatalyst when exposed to the visible light, through which an advanced oxidation process (AOP) takes place. The production of radicals like O$_2$• and •OH, which are necessary for the degradation of the dyes, is made facile by the presence of a lower E_g. Similar to how the positively charged holes generate the (OH$^-$) group by interacting the water molecule, the O$_2$ also interact with the e$^-$ present at the interface located in the conduction band for generating the radical (•O$_2$) [superoxide] [19][68]. Through photocatalytic degradation, the organic pollutant is mineralized with its reduction to the basic product like CO$_2$ and H$_2$O. It is noteworthy here that the reduction in the E_g and the hindrance in the photogenerated electron-hole pairs recombination due to Pani sensitization greatly affects the photo-activity [69]. Since the holes at this neutral pH generates the hydroxyl free radical (•OH) by interacting with the (OH) group [68].

Through photocatalytic degradation, the organic pollutant is mineralized with its reduction to the basic product like CO$_2$ and H$_2$O. Since the oxidizing agent completely degrades the organic compounds, it is noteworthy here that the generation of the hydroxyl free radical (OH) and the hindrance in the photogenerated electron-hole pairs recombination substantially affect the photocatalytic degradation process [69]. Initially, the generation of the electron-hole pairs is due to the absorption of visible wavelength by the photocatalyst corresponding to the band gap energy. There are two essential mode through which the organic pollutant is degraded by heterogeneous photocatalysis: (i) the oxidation of the organic pollutant simple product occurs through attacks by the hydroxyl free radical (HO•), or (ii) primary contact of the

photogenerated holes with the organic pollutants following a mechanism analogous to the photo-Kolbe reaction [70]. The hydroxyl fee radical attack is initiated when the conduction band electrons $e_{(CB)}^{-}$ which are photogenerated interacts with the oxygen. It generates the superoxide specie $O_2^{\cdot-}$ that neutralized by the proton H+ leading to the formation of short-lived hydrogen peroxide or hydroperoxyl radicals $HO_2^{\cdot}$ [71]. Afterwards, the oxygen and hydrogen peroxide are produced as a result of its breakdown. The positively charged holes $h_{(VB)}^{+}$ react with water to form hydroxyl free radicals, or they may also oxidize organic dyes directly. The breakdown of the Sunset yellow dye into simple molecules is brought on by the hydroxyl free radicals [72];

$$Catalyst + hv \rightarrow e_{(CB)}^{-} + h_{(VB)}^{+}$$

$$e_{(CB)}^{-} + O_2 \rightarrow O_2^{\cdot-}$$

$$h_{(VB)}^{+} + H_2O\ (H^+ + OH^-) \rightarrow H^+ + OH^{\cdot}$$

$$O_2^{\cdot-} + H^+ \rightarrow\ ^{\cdot}HO_2$$

$$2\ ^{\cdot}HO_2 \rightarrow H_2O_2 + O_2$$

$$H_2O_2 + e^- \rightarrow OH^{\cdot} + OH^-$$

$$R + OH^{\cdot} \rightarrow R^{\cdot} + H_2O$$

$$R + h_{(VB)}^{+} \rightarrow R^{\cdot+} \rightarrow Degraded\ Product$$

The photocatalytic performance of different photocatalysts have been listed in Table 5 in comparison to the results acquired from the ternary nanocomposite Pani/Ni-α-Fe2O3/CNT suggests that the considerable percent degradation has been achieved along with decrease in the optical band gap of the as prepared photocatalyst.

32

Table 5

Photocatalytic performance by different photocatalyst compared to ternary nanocomposite Pani/Ni-α-Fe$_2$O$_3$/CNT

Photocatalyst	Band gap (eV)	Dye	Percent degradation (%)	Ref.
Cobalt chromium oxide (CoCr$_2$O$_4$) nanoparticles	1.74	Congo Red	94	[73]
p-NiFe$_2$O$_4$/n-TiO$_2$ hetero-structure	NiFe$_2$O$_4$ (E_g =1.64 eV), TiO$_2$ (E_g = 3.21 eV)	Congo Red	97	[74]
Hetero-junction ZnMn$_2$O$_4$/TiO$_2$	ZnMn$_2$O$_4$ (E_g =1.97 eV), TiO$_2$ (E_g = 3.24 eV)	Rhodamine B	95	[75]
Bi(III) MOFs, including UU-200, CAU-17, and their integrated architecture, namely MIX-UCAU	~ 3.43 eV to 3.60 eV	Rhodamine B	~99	[76]
Cadmium ferrite (CdFe$_2$O$_4$) nanoparticles	1.71	Methyl green	~99	[12]
Pani/Ni-α-Fe$_2$O$_3$/CNT	1.32	Sunset yellow	98.42	This study

Modelling of degradation kinetics by the Langmuir-Hinshelwood Model [L-H]

The Langmuir-Hinshelwood model, which elaborates on its kinetics, properly explains the electron transport process that underlies photocatalytic degradation. According to the L-H model, the dye molecule is adsorbed in line with the Langmuir model prior to photodegradation. The adsorptive nature of the organic pollutant at the photocatalyst surface is the fundamental foundation of the Langmuir-Hinshelwood model [77]. The rate of degradation suggests a plausible interaction between the Sunset yellow dye and the photocatalyst surface that leads to a high rate of surface adsorption at various initial dye concentrations.
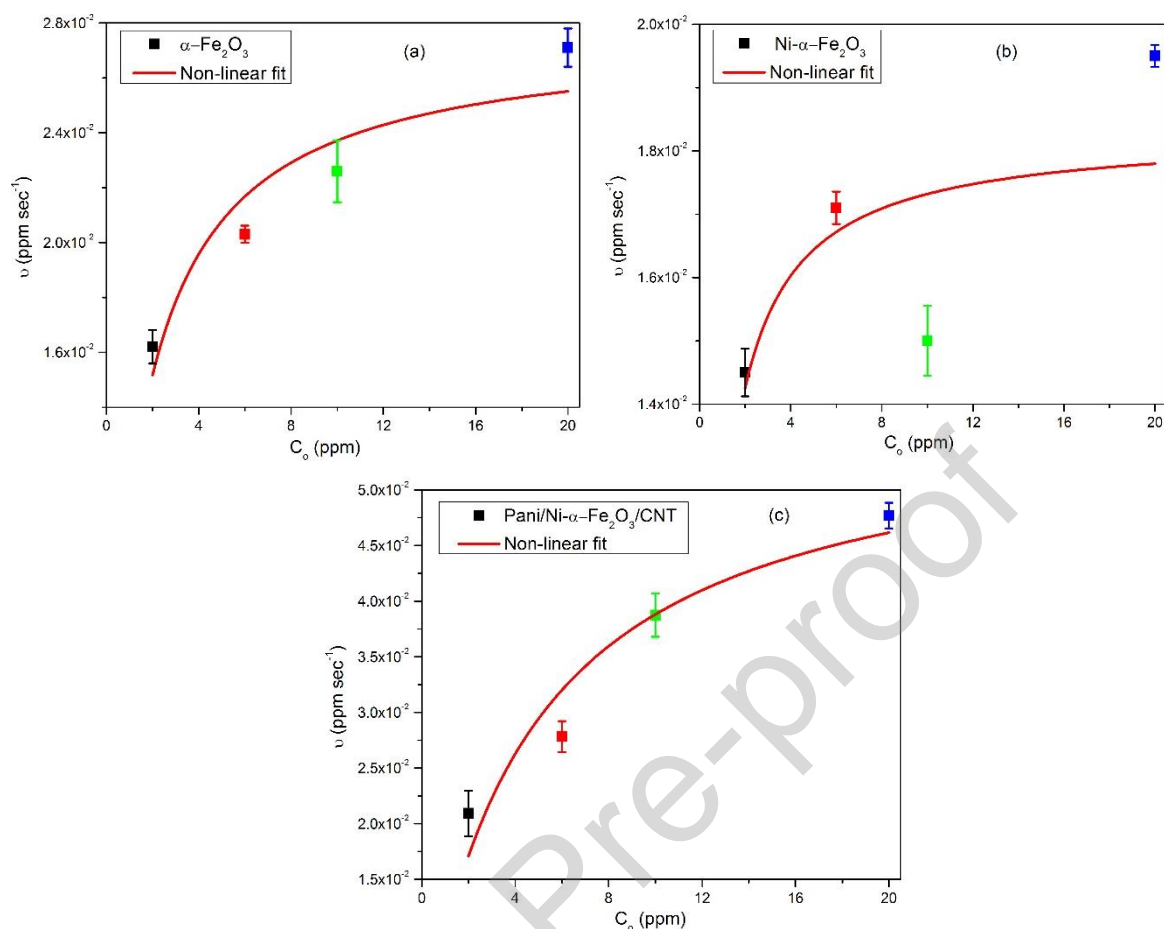
Fig. 12 Kinetic measurements of photocatalytic degradation for Sunset yellow dye fitted with non-linear Langmuir-Hinshelwood model for (a) α-Fe$_2$O$_3$ NPs, (b) Ni-α-Fe$_2$O$_3$ NPs (c) Pani/Ni-α-Fe$_2$O$_3$/CNT ternary nanocomposite.

As shown in Fig. 12, the non-linear Langmuir-Hinshelwood connection between the concentration of the Sunset yellow dye and the rate of photodegradation is as follows:

$$v = k_{app}C = \frac{k_r k_s C_o}{1 + k_s C_o} \quad \dots\dots\dots\dots\dots\dots\dots\dots\dots (10)$$

While the k_r (mg/L min) and k_s (L/mg) stands for the reaction rate and adsorption constants, accordingly.

Table 6

Kinetic parameters derived from non-linear Langmuir-Hinshelwood model

	α-Fe$_2$O$_3$ NPs	Ni-α-Fe$_2$O$_3$ NPs	Pani/Ni-α-Fe$_2$O$_3$/CNT
k_r (mg/L min)	0.0276	0.0183	0.0569
k_s (L/mg)	0.6102	1.7614	0.2142

34

The co-adsorption phenomenon is necessary for the photocatalytic activity because when two or more species adsorb on the catalyst surface, the presence of the secondary species may change the electronic structure of the surface. Such secondary species, which are the hydroxyl free radical (HO), which should primarily be produced by electron donation from the OH- and H_2O molecules to the photo excited holes, may be referred to as promoters when they boost the photocatalytic activity. At least one reactant undergoes chemisorption at the surface of the photocatalyst, which is followed by its transformation into a reactive form that reacts quickly, then desorption of the product is followed. This fact that the reaction rate is based on the surface coverage of the reacting species is elaborated by the surface phenomenon, which also involves the reactive interaction between the changed molecular fragments of the reactant molecules. As shown in Table 6, the ternary nanocomposite (PNFC) has a higher rate constant (k_r) than the α-Fe_2O_3 and Ni-α-Fe_2O_3 NPs because the Sunset yellow dye covers more surface area than the hydroxyl free radical (HO), which is constant because there is a large excess of OH- and H_2O molecules. However, the rate constant k_r is also influenced by the second order kinetic. Similar to that, the ternary nanocomposite's (PFG) adsorption constant k_s in Table 5 shows a higher concentration of the intermediate product of degradation due to an improvement in the photocatalytic activity [78].

Conclusions

In this systematic work, we analysed the correlation between the cathodic shift of the E_{onset} and lowering of the E_{fb} in conjunction with the redshift of the optical band gap E_g. To this end, our approach was post doping modification of α-Fe_2O_3 with Pani for the fabrication of the photoanodes. A cathodic shift in E_{fb} was observed from -0.493 V for α-Fe_2O_3 to -0.692 V for the ternary nanocomposite PNFC which were in correspondence to the decrease in their E_g from 1.76 eV to 1.32 eV, respectively. PEC measurements under dark and illumination pointed to fact that electron hole pair recombination has not only been hindered but the photogenerated

charge carriers mobility has also increased enhancing the electrochemical properties at the electrode/electrolyte interface. Mott–Schottky analysis revealed the n-type nature of the ternary nanocomposite PNFC. The photo activity results also confirm an enhancement in the utilization of solar irradiation which suggests that the ternary nanocomposite PNFC is an actively enhanced photoactive material. These results which are presented here depict the enhancement of the photo-optical properties of the α-Fe_2O_3 with post doping modification using Pani. It is because of the fact that it produced the electron-hole pair extensively whereas the carbon nanofillers effectively transferred the photo-excited carriers hindering the charge carrier recombination. This improvement in the photo-optical behavior corresponds to the optical band gap energy reduction as well as the hindrance in the electron-hole pair recombination.

References

[1] B. Iandolo, H. Zhang, B. Wickman, I. Zorić, G. Conibeer, A. Hellman, Correlating flat band and onset potentials for solar water splitting on model hematite photoanodes, RSC Adv. 5 (2015) 61021-61030.

[2] G. Burgeth, H. Kisch, Photocatalytic and photoelectrochemical properties of titania–chloroplatinate (IV), Coordin. Chem. Rev. 230 (2002) 41-47.

[3] T.U.H. Zia, A.U.H.A. Shah, Label-free photoelectrochemical immunosensor based on sensitive photocatalytic surface of Sn doped ZnO for detection of hepatitis C (HCV) anticore mAbs 19D9D6, Colloid Surface A 630 (2021) 127076.

[4] D. Macwan, P.N. Dave, S. Chaturvedi, A review on nano-TiO_2 sol–gel type syntheses and its applications, J. Mater. Sci. 46 (2011) 3669-3686.

[5] L. Messaadia, S. Kiamouche, H. Lahmar, R. Masmoudi, H. Boulahbel, M. Trari, M. Benamira, Solar photodegradation of Rhodamine B dye by Cu_2O/TiO_2 heterostructure: experimental and computational studies of degradation and toxicity, J. Mol. Model. 29 (2023) 38.

[6] F. Kayaci, S. Vempati, C.O. Akgun, I. Donmez I, N. Biyikli, T. Uyar, Selective isolation of the electron or hole in photocatalysis: $ZnO-TiO_2$ and TiO_2-ZnO core-shell structured heterojunction nanofibers via electrospinning and atomic layer deposition, Nanoscale 6 (2014) 5735-5745.

[7] T.u.H. Zia, S.F. Shah, A. ul Haq, B. Ara, K. Gul, Fabricating ternary α-Fe_2O_3 nanoparticles-Polyaniline-Graphite nanoplatelets nanocomposite with enhanced photoelectrochemical activity for potential use as peroxidase mimic as well as photocatalyst, J. Environ. Chem. Eng. (2023) 110410.

[8] A.A. Alqadami, M. Naushad, M.A. Abdalla, M.R. Khan, Z.A. Alothman, Adsorptive removal of toxic dye using Fe_3O_4–TSC nanocomposite: equilibrium, kinetic, and thermodynamic studies, J. Chem. Eng. Data 61 (2016) 3806-3813.

[9] G.K. Mor, H.E. Prakasam, O.K. Varghese, K. Shankar, C.A. Grimes, Vertically oriented Ti− Fe− O nanotube array films: toward a useful material architecture for solar spectrum water photoelectrolysis, Nano Lett. 7 (2007) 2356-2364.

[10] S.M. El-Sheikh, F.A. Harraz, K.S. Abdel-Halim, Catalytic performance of nanostructured iron oxides synthesized by thermal decomposition technique, J. Alloy. Compd. 487 (2009) 716-723.

[11] B. Gilbert, C. Frandsen, E. Maxey, D. Sherman, Band-gap measurements of bulk and nanoscale hematite by soft x-ray spectroscopy, Phys. Rev. B. 79 (2009) 035108.

[12] S. Douafer, H. Lahmar, R. Laouici, F. Akika, M. Trari, I. Avramova, M. Benamira, Synthesis and characterization of $CdFe_2O_4$ nanoparticles: Application for the removal of Methyl Green under solar irradiation, Mater. Today 35 (2023) 105630.

[13] J.-C. Chiang, A.G. MacDiarmid, 'Polyaniline': Protonic acid doping of the emeraldine form to the metallic regime, Synthetic Met. 13 (1986) 193-205.

[14] B. Butoi, C.S. Ciobanu, S.L. Iconaru, C.C. Negrilă, M.A. Badea, M. Balas, A. Dinischiotu, G. Predoi, B. Bita, A. Groza, Iron-Oxide-Nanoparticles-Doped Polyaniline Composite Thin Films, Polymers 14 (2022) 1821.

[15] J. Schultze, H. Karabulut, Application potential of conducting polymers, Electrochim. Acta 50 (2005) 1739-1745.

[16] T. Xu, L. Zhang, H. Cheng, Y. Zhu, Significantly enhanced photocatalytic performance of ZnO via graphene hybridization and the mechanism study, Appl. Catal. B: Environ. 101 (2011) 382-387.

[17] K. Dai, G. Dawson, S. Yang, Z. Chen, L. Lu, Large scale preparing carbon nanotube/zinc oxide hybrid and its application for highly reusable photocatalyst, Chem. Eng. J. 191 (2012) 571-578.

[18] H. Fu, T. Xu, S. Zhu, Y. Zhu, Photocorrosion inhibition and enhancement of photocatalytic activity for ZnO via hybridization with C60, Environ. Sci. Technol. 42 (2008) 8064-8069.

[19] K. Petcharoen, A. Sirivat, Synthesis and characterization of magnetite nanoparticles via the chemical co-precipitation method, Mater. Sci. Eng. B-Adv 177 (2012) 421-427.

[20] Y. El Mendili, J.-F.o. Bardeau, N. Randrianantoandro, F. Grasset, J.-M. Greneche, Insights into the mechanism related to the phase transition from γ-Fe$_2$O$_3$ to α-Fe$_2$O$_3$ nanoparticles induced by thermal treatment and laser irradiation, J. Phys. Chem. C 116 (2012) 23785-23792.

[21] I. Gul, W. Ahmed, A. Maqsood, Electrical and magnetic characterization of nanocrystalline Ni–Zn ferrite synthesis by co-precipitation route, J. Magn. Magn. Mater. 320 (2008) 270-275.

[22] T.U.H. Zia, A.N. Khan, B. Ara, K. Gul, Electrochemical Capacitance Properties of Electrode based on Polyaniline (PANI) coated Graphite Nano Platelets (GnP)/Polystyrene (PS) Composite Film, J. Electrochem. Energy 17 (2020) 1-33.

[23] I. Chernyshova, M. Hochella Jr, A. Madden, Size-dependent structural transformations of hematite nanoparticles. 1. Phase transition, Phys. Chem. Chem. Phys. 9 (2007) 1736-1750.

[24] Z. Jing, S. Wu, Synthesis and characterization of monodisperse hematite nanoparticles modified by surfactants via hydrothermal approach, Mater. Lett. 58 (2004) 3637-3640.

[25] A.B. Afzal, M.J. Akhtar, M. Nadeem, M. Hassan, Dielectric and impedance studies of DBSA doped polyaniline/PVC composites, Curr. Appl. Phys. 10 (2010) 601-606.

[26] N. Colak, B. Sökmen, Doping of chemically synthesized polyaniline, Des. Monomer. Polym. 3 (2000) 181-189.

[27] Q. Wang, Y. Wang, Q. Meng, T. Wang, W. Guo, G. Wu, L. You, Preparation of high antistatic HDPE/polyaniline encapsulated graphene nanoplatelet composites by solution blending, RSC Adv. 7 (2017) 2796-2803.

[28] Z. Ghebache, Z. Safidine, F. Hamidouche, N. Boudieb, A. Benaboura, M. Trari, Effect of Hematite on the Energy Storage Performance of Polyaniline/Zeolite HY/α-Fe$_2$O$_3$ Nanocomposite Supercapacitor Electrode, J. Inorg. Organomet. P. 31 (2021) 1153-1162.

[29] L. Hu, A. Percheron, D. Chaumont, C.-H. Brachais, Microwave-assisted one-step hydrothermal synthesis of pure iron oxide nanoparticles: magnetite, maghemite and hematite, J. Sol-gel Sci. Techn. 60 (2011) 198.

[30] M. Jozefowicz, R. Laversanne, H. Javadi, A. Epstein, J. Pouget, X. Tang, A. MacDiarmid, Multiple lattice phases and polaron-lattice—spinless-defect competition in polyaniline, Phys. Rev. B. 39 (1989) 12958.

[31] J. Pouget, C. Hsu, A. Macdiarmid, A. Epstien, Synthesis of iodine-capped aniline trimers and analysis of their electronic spectrum, Synthetic Met. 69 (1995) 119.

[32] J.I. Tariq Jan, M. Ismail, M. Zakaullah, S.H. Naqvi, N. Badshah, Sn doping induced enhancement in the activity of ZnO nanostructures against antibiotic resistant S. aureus bacteria, Int. J. Nanomed. 8 (2013) 3679.

[33] R.M. Cornell, U. Schwertmann, The iron oxides: structure, properties, reactions, occurrences, and uses, Wiley-vch, Weinheim, 2003.

[34] D.M. Sherman, T.D. Waite, Electronic spectra of Fe^{3+} oxides and oxide hydroxides in the near IR to near UV, Am. Mineral. 70 (1985) 1262-1269.

[35] M. Valášková, J. Tokarský, J. Pavlovský, T. Prostějovský, K. Kočí, α-Fe_2O_3 nanoparticles/vermiculite clay material: structural, optical and photocatalytic properties, Materials, 12 (2019) 1880.

[36] Y.-G. Han, T. Kusunose, T. Sekino, One-step reverse micelle polymerization of organic dispersible polyaniline nanoparticles, Synthetic Met. 159 (2009) 123-131.

[37] M. Meinert, G. Reiss, Electronic structure and optical band gap determination of $NiFe_2O_4$, J. Phys.: Condens. Mat. 26 (2014) 115503.

[38] H. Ning, X. Liu, H. Zhang, Z. Fang, W. Cai, J. Chen, R. Yao, M. Xu, L. Wang, L. Lan, Effect of intrinsic stress on structural and optical properties of amorphous Si-doped SnO_2 thin-film, Materials, 10 (2017) 24.

[39] S.K. O'Leary, Optical absorption, disorder, and the disorderless limit in amorphous semiconductors, Appl. Phys. Lett. 72 (1998) 1332-1334.

[40] Z. Gan, S. Xiong, X. Wu, T. Xu, X. Zhu, X. Gan, J. Guo, J. Shen, L. Sun, P.K. Chu, Mechanism of photoluminescence from chemically derived graphene oxide: role of chemical reduction, Adv. Opt. Mater. 1 (2013) 926-932.

[41] T. Somesh, M.Q. Al-Gunaid, B. Madhukar, Photosensitization of optical band gap modified polyvinyl alcohol films with hybrid $AgAlO_2$ nanoparticles, Journal of Materials Science: Mater. Electron. 30 (2019) 37-49.

[42] F. Urbach, The long-wavelength edge of photographic sensitivity and of the electronic absorption of solids, Phys. Rev. 92 (1953) 1324.

[43] G.H. Brilmyer, A.J. Bard, Electrogenerated Chemiluminescence: XXXVI. The Production of Steady Direct Current ECL in Thin Layer and Flow Cells, J. Electrochem. Soc. 127 (1980) 104.

[44] M. Quintana, T. Edvinsson, A. Hagfeldt, G. Boschloo, Comparison of dye-sensitized ZnO and TiO_2 solar cells: studies of charge transport and carrier lifetime, J. Phys. Chem. C. 111 (2007) 1035-1041.

[45] J. Deng, X. Lv, K. Nie, X. Lv, X. Sun, J. Zhong, Lowering the onset potential of Fe_2TiO_5/Fe_2O_3 photoanodes by interface structures: F-and Rh-based treatments, ACS Catal. 7 (2017) 4062-4069.

[46] P.S. Bassi, L.H. Wong, J. Barber, Iron based photoanodes for solar fuel production, Phys. Chem. Chem. Phys. 16 (2014) 11834-11842.

[47] Q. Tang, W. Wang, G. Wang, The perfect matching between the low-cost Fe_2O_3 nanowire anode and the NiO nanoflake cathode significantly enhances the energy density of asymmetric supercapacitors, J. Mater. Chem. A. 3 (2015) 6662-6670.

[48] V. Subramanian, E.E. Wolf, P.V. Kamat, Catalysis with TiO$_2$/gold nanocomposites. Effect of metal particle size on the Fermi level equilibration, J. Am. Chem. Soc. 126 (2004) 4943-4950.

[49] Y. Ma, P.S. Shinde, X. Li, S. Pan, High-throughput screening and surface interrogation studies of Au-modified hematite photoanodes by scanning electrochemical microscopy for solar water splitting, ACS Omega 4 (2019) 17257-17268.

[50] M. Grätzel, Photoelectrochemical cells, Nature 414 (2001) 338-344.

[51] G. Hodes, I. Howell, L. Peter, Nanocrystalline photoelectrochemical cells: a new concept in photovoltaic cells, J. Electrochem. Soc. 139 (1992) 3136.

[52] K.-K. Kim, H.-S. Kim, D.-K. Hwang, J.-H. Lim, S.-J. Park, Realization of p-type ZnO thin films via phosphorus doping and thermal activation of the dopant, Appl. Phys. Lett. 83 (2003) 63-65.

[53] F. Cardon, W. Gomes, On the determination of the flat-band potential of a semiconductor in contact with a metal or an electrolyte from the Mott-Schottky plot, J. Phys. D Appl. Phys. 11 (1978) L63.

[54] J. Dewald, The charge distribution at the zinc oxide-electrolyte interface, J. Phys. Chem. Solids 14 (1960) 155-161.

[55] A.J. Bard, L.R. Faulkner, J. Leddy, C.G. Zoski, Electrochemical methods: fundamentals and applications, Wiley, New York, 1980.

[56] P.S. Shinde, S.H. Choi, Y. Kim, J. Ryu, J.S. Jang, Onset potential behavior in α-Fe$_2$O$_3$ photoanodes: the influence of surface and diffusion Sn doping on the surface states, Phys. Chem. Chem. Phys. 18 (2016) 2495-2509.

[57] A. Yamakata, J.J.M. Vequizo, M. Kawaguchi, Behavior and energy state of photogenerated charge carriers in single-crystalline and polycrystalline powder SrTiO$_3$ studied by time-resolved absorption spectroscopy in the visible to mid-infrared region, J. Phys. Chem. C 119 (2015) 1880-1885.

[58] J. Zhang, J.H. Bang, C. Tang, P.V. Kamat, Tailored TiO$_2$−SrTiO$_3$ heterostructure nanotube arrays for improved photoelectrochemical performance, ACS Nano, 4 (2010) 387-395.

[59] W.-S. Chang, C.-C. Wu, M.-S. Jeng, K.-W. Cheng, C.-M. Huang, T.-C. Lee, Ternary Ag–In–S polycrystalline films deposited using chemical bath deposition for photoelectrochemical applications, Mater. Chem. Phys. 120 (2010) 307-312.

[60] Z. Zhang, J.T. Yates Jr, Band bending in semiconductors: chemical and physical consequences at surfaces and interfaces, Chem. Rev. 112 (2012) 5520-5551.

[61] A. Hagfeldt, U. Björkstén, M. Grätzel, Photocapacitance of nanocrystalline oxide semiconductor films: band-edge movement in mesoporous TiO$_2$ electrodes during UV illumination, J. Phys. Chem. 100 (1996) 8045-8048.

[62] A.J. Bard, Photoelectrochemistry and heterogeneous photocatalysis at semiconductors, J. Photochem. 10 (1979) 59-75.

[63] S. Zehra, H. Lgaz, A. Chaouiki, H. Serrar, S. Kaya, R. Salghi, S. AbdelRaheem, S. Boukhris, A. Guenbour, I.-M. Chung, Evaluation of inhibitive and adsorption behavior of thiazole-4-carboxylates on mild steel corrosion in HCl, Colloid Surface A 606 (2020) 125351.

[64] Z. Huang, P. Zhong, C. Wang, X. Zhang, C. Zhang, Silicon nanowires/reduced graphene oxide composites for enhanced photoelectrochemical properties, ACS Appl. Mater. Inter. 5 (2013) 1961-1966.

[65] D. Merki, H. Vrubel, L. Rovelli, S. Fierro, X. Hu, Fe, Co, and Ni ions promote the catalytic activity of amorphous molybdenum sulfide films for hydrogen evolution, Chem. Sci. 3 (2012) 2515-2525.

[66] J. Miao, A. Xie, S. Li, F. Huang, J. Cao, Y. Shen, A novel reducing graphene/polyaniline/cuprous oxide composite hydrogel with unexpected photocatalytic activity for the degradation of Congo red, Appl. Surf. Sci. 360 (2016) 594-600.

[67] Y. Tang, N. Wu, S. Luo, C. Liu, K. Wang, L. Chen, One-Step Electrodeposition to Layer-by-Layer Graphene–Conducting-Polymer Hybrid Films, Macromol. Rapid Comm. 33 (2012) 1780-1786.

[68] Y. Deng, R. Zhao, Advanced oxidation processes (AOPs) in wastewater treatment, Curr. Poll. Rep. 1 (2015) 167-176.

[69] C. Pan, Y. Zhu, New type of $BiPO_4$ oxy-acid salt photocatalyst with high photocatalytic activity on degradation of dye, Environ. Sci. Technol. 44 (2010) 5570-5574.

[70] B. Kraeutler, A.J. Bard, Photoelectrosynthesis of ethane from acetate ion at an n-type titanium dioxide electrode. The photo-Kolbe reaction, J. Am. Chem. Soc. 99 (1977) 7729-7731.

[71] L.M. Ahmed, Bulk and Nanocatalysts Applications in Advanced Oxidation Processes, in: Oxidoreductase, BoD–Books on Demand: Norderstedt, Germany, 2021.

[72] M. Pawar, S. Topcu Sendoğdular, P. Gouma, A brief overview of TiO_2 photocatalyst for organic dye remediation: case study of reaction mechanisms involved in Ce-TiO_2 photocatalysts system, J. Nanomater. 2018 (2018) 5953609.

[73] D. Chaibeddra, M. Benamira, M. Colmont, H. Boulehbal, H. Lahmar, I. Avramova, M. Trari, Synthesis, physical and electrochemical characterization of $CoCr_2O_4$ and its application as photocatalyst under solar irradiation, Inorg. Chem. Commun. (2023) 111116.

[74] H. Boulahbel, M. Benamira, F. Bouremmad, N. Ahmia, S. Kiamouche, H. Lahmar, A. Souici, M. Trari, Enhanced photodegradation of Congo red dye under sunlight irradiation by pn NiFe2O4/TiO2 heterostructure, Inorg. Chem. Comm. 154 (2023) 110921.

[75] N. Ahmia, M. Benamira, L. Messaadia, M. Colmont, H. Boulahbel, H. Lahmar, A. Souici, M. Trari, Photocatalytic activity of $ZnMn_2O_4$/TiO_2 heterostructure under solar light irradiation: Experimental and theoretical study, J. Mol. Struct. 1306 (2024) 137834.

[76] H.A. Le Pham, D.T. Nguyen, V.C. Nguyen, T.K. Vo, Integrating Bi-containing metal–organic frameworks for enhancing their LED visible-light-driven photocatalytic activities towards Rhodamine dye, Inorg. Chem. Commun. 159 (2024) 111822.

[77] M. Behnajady, N. Modirshahla, R. Hamzavi, Kinetic study on photocatalytic degradation of CI Acid Yellow 23 by ZnO photocatalyst, J. Hazard. Mater. 133 (2006) 226-232.

[78] P. Atkins, P.W. Atkins, J. de Paula, Atkins' physical chemistry, Oxford university press, Oxford, 2014.

Graphical abstract
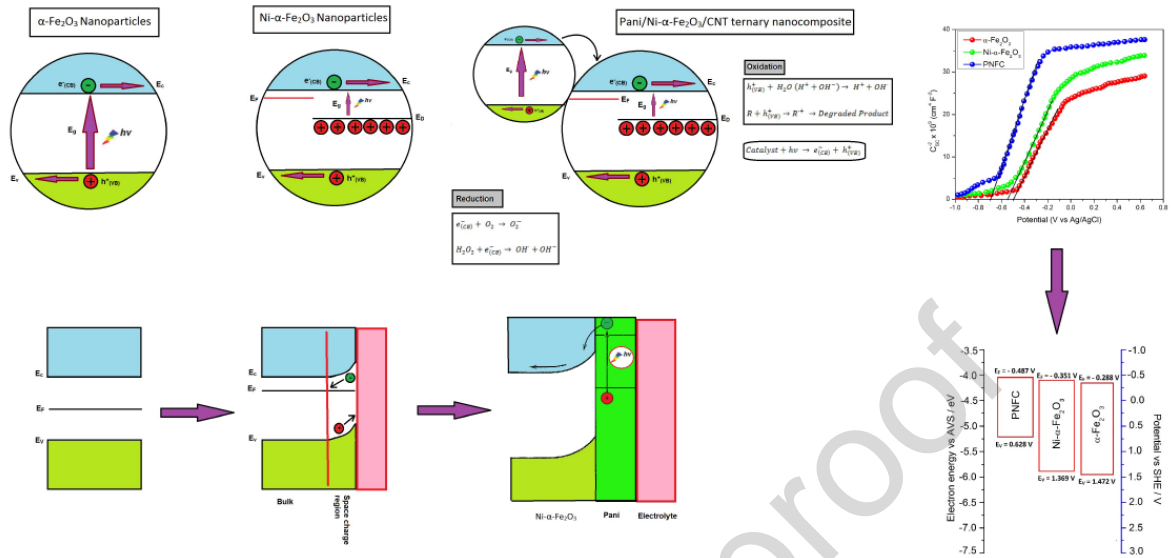
Declaration of interests

☑The authors declare that they have no known competing financial interests or personal relationships that could have appeared to influence the work reported in this paper.

☐ The authors declare the following financial interests/personal relationships which may be considered as potential competing interests:

Highlights

- Hematite (α-Fe$_2$O$_3$) based ternary nanocomposite PNFC was prepared using Ni doped α-Fe$_2$O$_3$ and polyaniline to fabricate a photoactive material.

- The optical band gap (E_g) analysis, Mott–Schottky analysis and electrochemical impedance spectroscopy established a quantitative relationship between the band gap reduction (redshift) and negative shift of E_{fb}.

- The optical band gap (E_g) values clearly showed decrease in the optical band gap from 1.76 eV for α-Fe$_2$O$_3$ to 1.32 eV for PNFC pertaining to the photosensitization of the Ni-α-Fe$_2$O$_3$ NPs through functionalization with Pani.

- The cathodic shift in onset potential (E_{onset}) and negative shift in flat band potential (E_{fb}) was observed for ternary nanocomposite PNFC.

- It was observed that the E_{onset} value of -0.457 V for α-Fe$_2$O$_3$ based electrode shifted to -0.638 V for ternary nanocomposite (PNFC) based electrode.